JBC RESEARCH ARTICLE

Mechanisms by which small molecules of diverse chemotypes arrest Sec14 lipid transfer activity

Received for publication, November 5, 2022, and in revised form, December 27, 2022 Published, Papers in Press, January 2, 2023,
https://doi.org/10.1016/j.jbc.2022.102861

Xiao-Ru Chen[1], Lokendra Poudel[1], Zebin Hong[2], Philipp Johnen[3], Sachin Katti[1], Ashutosh Tripathi[4], Aaron H. Nile[4], Savana M. Green[1,4], Danish Khan[1], Gabriel Schaaf[3], Fulvia Bono[2], Vytas A. Bankaitis[1,4,*], and Tatyana I. Igumenova[1,*]

From the [1]Department of Biochemistry & Biophysics, Texas A&M University, College Station, Texas USA; [2]Max Planck Institute for Developmental Biology, Tübingen, Germany; [3]Institute for Crop Science and Resource Conservation, Universität Bonn, Bonn, Germany; [4]Department of Cell Biology & Genetics, Texas A&M University, College Station, Texas, USA

Edited by Alex Toker

Phosphatidylinositol (PtdIns) transfer proteins (PITPs) enhance the activities of PtdIns 4-OH kinases that generate signaling pools of PtdIns-4-phosphate. In that capacity, PITPs serve as key regulators of lipid signaling in eukaryotic cells. Although the PITP phospholipid exchange cycle is the engine that stimulates PtdIns 4-OH kinase activities, the underlying mechanism is not understood. Herein, we apply an integrative structural biology approach to investigate interactions of the yeast PITP Sec14 with small-molecule inhibitors (SMIs) of its phospholipid exchange cycle. Using a combination of X-ray crystallography, solution NMR spectroscopy, and atomistic MD simulations, we dissect how SMIs compete with native Sec14 phospholipid ligands and arrest phospholipid exchange. Moreover, as Sec14 PITPs represent new targets for the development of next-generation antifungal drugs, the structures of Sec14 bound to SMIs of diverse chemotypes reported in this study will provide critical information required for future structure-based design of next-generation lead compounds directed against Sec14 PITPs of virulent fungi.

Phosphoinositides are phosphorylated derivatives of phosphatidylinositol (PtdIns) that, along with their metabolic byproducts (*e.g.*, diacylglycerol and soluble inositol-phosphates), regulate an impressively broad set of intracellular activities in all eukaryotic cells (1–4). As such, phosphoinositides represent the foundation of a major intracellular signaling pathway. Indeed, the 4-OH and 4,5-OH–phosphorylated phosphatidylinositol derivatives phosphatidylinositol-4-phosphate (PtdIns-4-P) and PtdIns-4,5-bisphosphate are essential for viability at the single cell level across the *Eukaryota*. PtdIns-4-P synthesis in particular is subject to an unusual mode of regulation. The PtdIns 4-OH kinases that produce this phosphoinositide must be simulated by phosphatidylinositol transfer proteins (PITPs) to power biologically sufficient thresholds of PtdIns-4-P signaling.

PITPs fall into two structurally unrelated families characterized by the Sec14 and the START (StAR-related lipid transfer) protein folds. PITP deficiencies of either family are associated with striking phenotypes in fungi, plants, insects, and vertebrates (5–14). The yeast Sec14, the founding member of the extensive Sec14 protein family (15, 16), is the focus of this work. Sec14 is a PtdIns and phosphatidylcholine (PtdCho) exchange protein that exhibits high binding specificity for these lipids *in vivo* and *in vitro*, and whose PtdIns/PtdCho exchange activities are essential for the PtdIns-4-P–dependent membrane trafficking from the yeast trans-Golgi network (TGN) (5, 6, 16, 17). It is on this basis that the membrane trafficking activities of Sec14 orthologs are essential for the virulence of pathogenic fungi of clinical significance (18, 19). When coupled with demonstrations that small molecules directly inhibit yeast Sec14 with exquisite specificity with no obvious off-target effects (20–22), the emerging data identify Sec14 as an attractive target for development of next-generation antifungal drugs (23–26). This attractiveness is further justified by the fact that mammalian Sec14-like proteins lack the motifs critical for binding to presently validated small molecule inhibitors directed against fungal Sec14 PITPs (25, 26).

Current models posit yeast Sec14 and its homologs stimulate PtdIns 4-OH kinase activities by rendering PtdIns a more accessible substrate for these enzymes. PtdIns 4-OH kinases are intrinsically poor interfacial enzymes incapable of overcoming the actions of PtdIns-4-P signaling antagonists. The heterotypic PtdIns/PtdCho exchange cycle represents the engine that potentiates PtdIns 4-OH kinase activity *in vivo* (17, 27). Given the biological importance of Sec14, and its pharmacological potential in the antifungal drug arena, it is therefore essential to develop a full mechanistic understanding of the Sec14 lipid exchange cycle that lies at the core of PITP function.

A model depicting the heterotypic PtdIns/PtdCho exchange cycle is illustrated in Figure 1 where Sec14 exchanges PtdCho for PtdIns on TGN membranes. The exchange process is initiated by Sec14 recruitment from the cytoplasm to the TGN surface (Fig. 1*A* step 1). It is presently thought that the major Sec14 conformer in solution is a closed one where bound lipid is shielded from the aqueous environment (28) and that it is this conformer which engages TGN membranes (Fig. 1*B*; structure inferred from homology models of crystal structures

* For correspondence: Tatyana I. Igumenova, Tatyana.Igumenova@ag.tamu.edu; Vytas A. Bankaitis, vytas@tamu.edu.

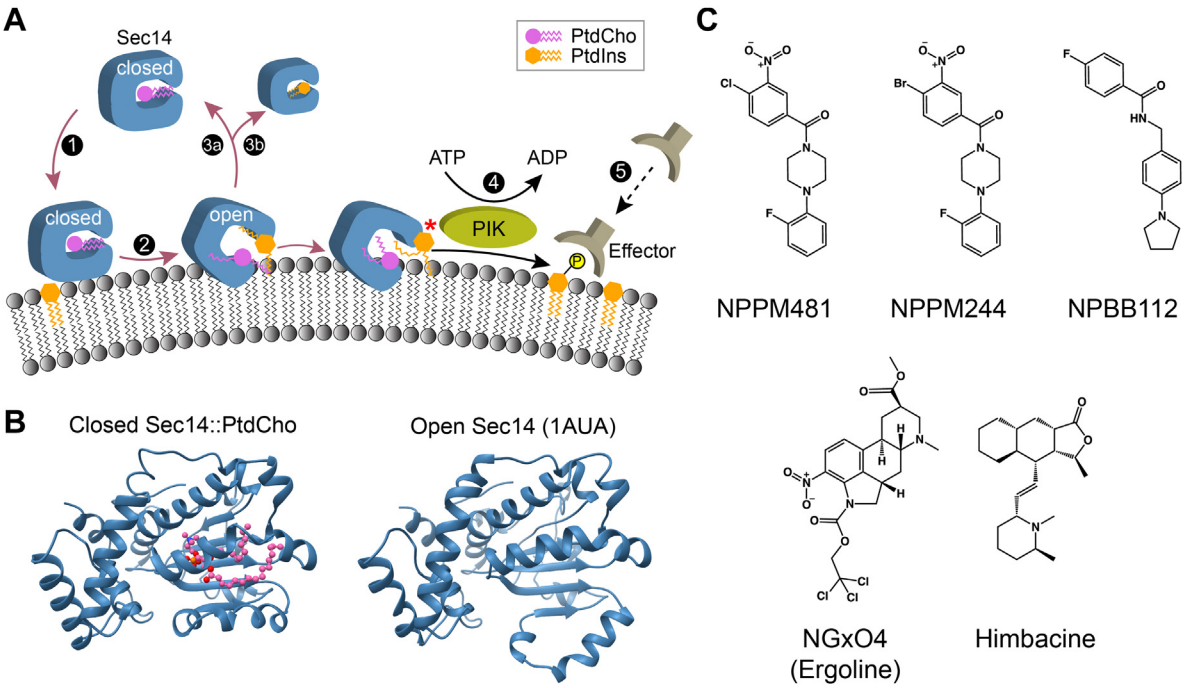

Figure 1. The Sec14 phospholipid exchange cycle potentiates PtdIns-4-P production. *A*, PtdIns presentation model for Sec14-mediated regulation of PtdIns-4-P signaling. PtdIns 4-OH kinases are biologically insufficient interfacial enzymes that cannot produce sufficient PtdIns-4-P to overcome the action of antagonists of PtdIns-4-P signaling. Recruitment of lipid-bound Sec14 (PtdCho-bound form is shown) to trans-Golgi network membranes (1) activates a PtdIns/PtdCho exchange cycle (2). PtdIns/PtdCho exchange ultimately results in Sec14 disengagement from membranes in either a PtdCho (3a) or PtdIns-bound form (3b) after which another round of recruitment/lipid exchange follows. Execution of a heterotypic PtdCho/PtdIns lipid exchange cycle renders PtdIns (marked with an *asterisk*) a superior substrate for PtdIns 4-OH kinase (PIK) (4). In this manner, Sec14 stimulates lipid kinase activity such that sufficient PtdIns-4-P is generated to produce a biologically actionable signal. *B*, the transition between the closed and open conformation of Sec14 is essential for the lipid exchange cycle. The Sec14 open conformation is represented in the crystal structure (PDB entry, 1AUA), while the closed conformation is modeled on the closed conformer crystal structure of the close Sec14 paralog Sfh1 complexed with PtdCho (3B7Z). *C*, Sec14-directed small molecule inhibitors of four distinct chemotypes. Chemical structures of the 4-chloro- and 4-bromo-3-nitrophenyl)(4-(2-methoxyphenyl)piperazin-1-yl)methanones NPPM481 and NPPM244, respectively, the 4-fluoro-N-[4-(1-pyrrolidinyl)benzyl]benzamide) NPBB112, the ergoline NGx04, and the piperidine alkaloid natural product himbacine are shown. These SMIs inhibit the Sec14 phospholipid exchange cycle. PtdIns, phosphatidylinositol; PtdIns-4-P, phosphatidylinositol-4-phosphate; PtdCho, phosphatidylcholine; SMI, small-molecule inhibitor.

of closed lipid-bound conformers of the close Sec14 paralog and functional surrogate Sfh1; (17, 29)). Sec14 is proposed to subsequently transition to an open conformer permissive for concerted egress of bound phospholipid and uptake of a phospholipid ligand from the bilayer (Fig. 1*A*, step 2; structure inferred from crystal structures of β-octylglucopyranoside–bound open Sec14 conformers; (30, 31)). Multiple rounds of lipid exchange can occur until a turn of the exchange cycle results in disengagement of a closed lipid-bound Sec14 conformer from the membrane surface (Fig. 1*A*, steps 3a or 3b). However, it is in the course of abortive PtdIns/PtdCho exchanges that Sec14 is posited to function as a PtdIns-presentation module that stimulates PtdIns-4-P synthesis (Fig. 1*A*, step 4). This functional partnership between Sec14 and PtdIns 4-OH kinase translates into a PtdCho-based metabolic input that potentiates membrane trafficking from the yeast TGN *via* activation of effectors that drive downstream PtdIns-4-P signaling (Fig. 1*A*, step 5).

The model illustrated in Figure 1, while informed by a wealth of functional *in vivo* and *in vitro* data, does not adequately describe the protein conformational transitions and lipid dynamics that define the mechanism of the Sec14 lipid exchange cycle. That information is essential for understanding how Sec14 potentiates PtdIns 4-OH kinase activities and regulates PtdIns-4-P signaling, and it is further required for realizing the potential of fungal Sec14 PITPs as targets for the development of urgently needed next-generation anti-mycotics. To address fundamental questions regarding operation of the Sec14 lipid exchange cycle, we investigate the underlying mechanisms of Sec14 inhibition by small-molecule inhibitors (SMIs) of four distinct chemotypes (Fig. 1*C*). All Sec14-directed SMIs studied in this work are potent inhibitors of PtdIns transfer activity *in vitro*: NPPM244 (IC_{50} = 0.1 μM) > NPPM481 (IC_{50} = 0.2 μM) > NPBB112 (IC_{50} = 1.0 μM) > himbacine (IC_{50} = 1.2 μM) (20, 32). NGxO4 (subsequently referred to ergoline) potency in that assay has not been determined, but the relative NGxO4 IC_{50} in yeast growth assays suggest it a less potent Sec14 inhibitor (33). Virtual dock models of Sec14 bound to NPPM481 and ergoline have been described and assessed by rational mutagenesis strategies (20, 33). However, these dock models fail to account for why specific polymorphisms in the lipid-binding cavities of virulent fungal Sec14 orthologs make these PITPs resistant to inhibition by 4-bromo- and 4-chloro-3-nitrophenyl)(4-(2-methoxyphenyl)piperazin-1-yl)methanones (NPPMs) and ergoline (21).

Using an integrative structural approach consisting of X-ray crystallography, atomistic molecular dynamics (MD) simulations, and fluorine-19 NMR (^{19}F NMR) spectroscopy, we describe how: (i) Sec14 binds SMIs of distinct chemotypes, (ii) the pathways by which SMIs interact with Sec14, and (iii) the conformational dynamics that accompany the Sec14 ligand exchange cycle. The deployment of these SMIs as tool compounds not only provides unprecedented insights into the operations of the Sec14 lipid exchange cycle, but also informs rational design of next-generation anti-mycotics that target Sec14 PITPs of virulent fungi.

Results

SMIs invade the Sec14 lipid-binding pocket

To define the structural basis for how Sec14 binds chemically diverse SMIs, and to understand mechanisms of resistance, the Sec14::SMI complexes were crystallized and their X-ray structures determined. The high resolution of these structures (2.3 Å: NPPM481, 2.1 Å: NPPM244, 2.7 Å: NPBB112, 2.3 Å: ergoline, and 1.8 Å: himbacine) provide precise descriptions of SMI-binding modes.

All five SMIs are sequestered in a common envelope of 21 amino acids that forms an amphiphilic subregion deep within the Sec14 lipid-binding cavity (Fig. 2*A*). Comparative structural analyses of Sec14::SMI and lipid complexes of its paralog (Sfh1::PtdCho and Sfh1::PtdIns) report on how these small molecules interfere with native ligand binding. We use NPPM481 as a representative for the NPPM/NPBB SMIs because NPPM481 and NPPM244 differ only in the identity of the A-ring halide substituent and hence share essentially identical binding modes within the Sec14 lipid-binding cavity. The NPBB112 binding mode also deviates in only minor respects (Fig. S1, *A*–*C*). We find that the NPPM481 B- and C-rings invade the binding space occupied by the glycerol backbone/proximal regions of the PtdCho *sn*-2 acyl chain and the proximal half of the PtdIns *sn*-2 acyl chain (Fig. 2*B*, left panel). By comparison, the ergoline-fused rings occlude PtdCho glycerol backbone/phosphoester and PtdIns glycerol backbone/proximal *sn*-2 acyl chain–binding environments (Fig. 2*B*, center panel). The himbacine ABC ring pose sterically clashes with that of the PtdCho headgroup, whereas the D-ring invades the space that accommodates the proximal halves of the PtdCho and PtdIns *sn-2* acyl chains (Fig. 2*D*, right panel). Of the four chemotypes, the himbacine molecule is set much shallower in the collective SMI binding environment, thereby leaving vacant the well-defined subpocket that accommodates the aryl halide and carboxylic ester groups of the NPPM/NPBB and ergoline SMIs (Fig. S1*G*).

The backbone of Sec14 in the crystalline complexes adopts an 'open' conformation with pairwise RMSDs relative to the apo Sec14 (PDB entry 1AUA) ranging from 0.6 to 1.2 Å

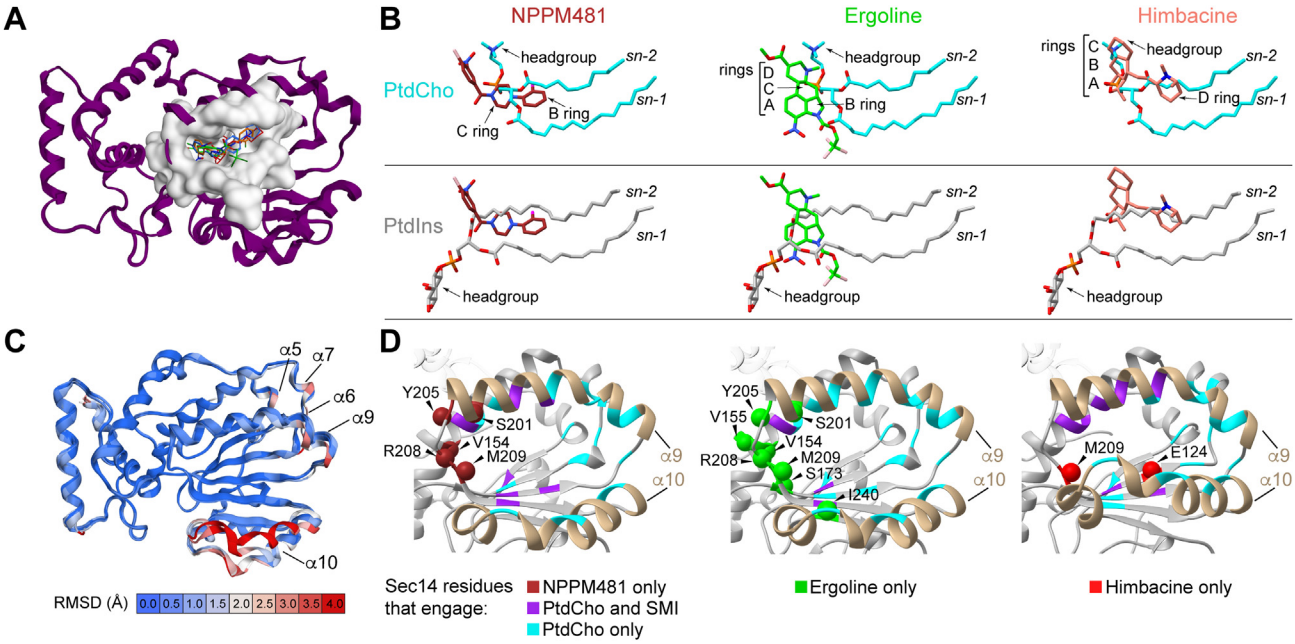

Figure 2. Small molecule inhibitors bind deep within the Sec14 lipid binding cavity. *A*, overlay of the binding poses of the five SMIs in the context of the Sec14 fold are shown. Highlighted in space-fill render is a 21 amino acid SMI-binding envelope that accommodates SMIs of all four chemotypes. The NPPM481, NPBB112, ergoline, and himbacine backbones are in *maroon*, *blue*, *green*, and *red*, respectively. Cl and F atoms are shown in *pink* and *magenta*, respectively. NPPM244 is not represented in the overlay as it superposes precisely onto the NPPM481 pose. *B*, comparison of the SMIs, PtdCho, and PtdIns binding poses. The backbone atoms of the Sec14::NPPM481, Sec14::ergoline, and Sec14::himbacine are superposed onto Sfh1::PtdCho and Sfh1::PtdIns, respectively. Only ligands are shown for clarity. Note that PDB entry 3B7Z was used to generate the lipid-binding poses containing both Sfh1::PtdCho and Sfh1::PtdIns complexes. *C*, per-residue RMSD values, color-coded and mapped onto each of the Sec14::SMI crystal structures. The apo Sec14 that crystallizes as an open conformer (PDB entry, 1AUA) is used as reference. α-Helices that include regions with significant RMSD values are labeled. Color-coded scale bar is at the bottom. *D*, ribbon representations of open Sec14 lipid-binding cavities of the Sec14::NPPM481 (*left*), Sec14::ergoline (*center*), and Sec14::himbacine complexes (*right*) are shown. The α9 and α10 helices that gate entry to the cavity are labeled. Beads mark residues that contact SMI only and the identities of those residues are shown. Regions that engage both SMI and PtdCho are colored in *purple* in the ribbon diagram, whereas those that engage only PtdCho are shown in *cyan*. PtdIns, phosphatidylinositol; PtdCho, phosphatidylcholine; SMI, small-molecule inhibitor.

(Fig. 2*C*). Moderate deviations from the apo reference structure are found in the helical regions α5-α7 and the N-terminal segment of helix α9. The largest deviations are observed in the helical "gate" element α10 whose conformational rearrangement is at the heart of the 'closed-to-open' Sec14 transition, and who showed considerable dynamics in previously conducted MD simulations (17, 30, 34). The structural variability of these regions does not bear significant consequences for the protein–SMI interaction patterns because the overwhelming majority of interacting residues reside on the superimposable regions.

Detailed analyses of protein-ligand hydrogen bonds and hydrophobic contacts identified the SMI-interacting residues of Sec14 (Fig. S1, *A–F*), and these were compared to the cohort of residues that interact with PtdCho in the Sec14 ortholog Sfh1 (Fig. 2*D*). These Sfh1 residues are an accurate proxy for the corresponding PtdCho-interacting residues of Sec14 (17). While there is considerable overlap (color-coded purple in Fig. 2*D*), there also exist "unique" Sec14 residues that interact only with SMIs. These are highlighted using SMI-specific color-coding and bead representation in Figure 2*D*. Of all chemotypes, ergoline and himbacine engage in the most and least number of unique interactions, respectively. A common pattern among NPPM/NPBB/ergoline SMIs is engagement with Ser_{201}, Tyr_{205}, Arg_{208}, and Met_{209} that reside in the C-terminal region of helix α9 and the adjacent loop. Met_{209} also interacts with himbacine. Our data indicate that while SMIs engage several key lipid-binding residues in Sec14, these inhibitors also form unique interactions within the lipid-binding cavity that likely contribute to their high-affinity interactions with Sec14.

Structural basis for how Sec14 accommodates SMIs of different chemotypes

Extended linear arrangements of rings (NPPM/NPBB), compact fused ring structures (himbacine), and fused rings derivatized with ester-linked extensions (ergoline) are all accommodated within the Sec14 lipid-binding cavity. To determine the underlying basis for this versatility, a detailed analysis of all Sec14–SMI interactions was carried out. The full description is given in the Supporting Information. Here, we emphasize the key outcomes of this analysis using Figure 3 as a guide. To facilitate the presentation of major results, each SMI was divided into three substructures (proximal, middle, distal) according to its molecular geometry and approximate position relative to the Val_{154}-Val_{155} motif (subsequently referred to as 'VV-motif'). This motif is a key determinant in Sec14 sensitivity to inhibition by SMIs (21).

First, there is extensive chemical complementarity between the hydrophobic/hydrophilic subregions of the Sec14 lipid-binding cavity and the apolar/polar regions of SMIs (SMI column, Figure 3, *A–C*). Hydrophobic subregions of the Sec14 cavity accommodate the SMI methyl groups, apolar ring structures, and halogen substituents, while the hydrophilic regions engage in polar interactions with the oxygen and nitrogen atoms of the SMIs. Of note, H-bonds do not dominate SMI-binding profiles as the contact mode of each SMI analyzed involves at most one H-bond interaction with protein (Fig. S1, *A–E*). The majority of the polar backbone atoms are sequestered in intraprotein hydrogen bonds and are not involved in SMI interactions (Fig. S3).

Second, the proximal regions of NPPMs, NPBB112 (Fig. S2*A*), and ergoline opportunistically invade a mostly hydrophobic pocket lined by the 'VV-motif', the sidechain methylenes of Arg_{208} and Tyr_{205}, and the Tyr_{151} ring (Fig. 3, *D–F*, 'proximal' column). This pocket (subsequently referred to as the VV-motif pocket) is adjacent to, but does not overlap, the PtdCho headgroup-binding space (Fig. 2*B*). The NPPM481 A-ring is anchored to the VV-motif pocket *via* π-π stacking and 'edge-on' halogen-π interactions (35) with the Tyr_{151} sidechain. The nitro group is engaged in polar interactions with Ser_{173} and also forms a hydrogen bond with the Tyr_{111} hydroxyl (Fig. S1*C*). In contrast to the other SMIs, the proximal himbacine 'BC' ring system is sandwiched between two aromatic rings of Tyr_{151} and Tyr_{122} and is far removed from the 'VV-motif'. This arrangement is of consequence to the ability of himbacine to inhibit Sec14 PITPs with amino acid substitutions in the VV-motif. [^{3}H]-PtdIns-transfer assays clamped at 287 nM PITP and 20 μM himbacine demonstrated that himbacine inhibited Sec14, $Sec14^{V154F}$, and $Sec14^{V155F}$ activities similarly (77 ± 1.3%, 71 ± 1.2%, and 73 ± 2.1% inhibition relative to mock controls, respectively). Mock controls supported total [^{3}H]-PtdIns-transfer that ranged from 16 to 28% with input [^{3}H]-PtdIns and assay backgrounds ranging from 7410 to 12125 cpm and 530 to 870 cpm, respectively. By contrast, [^{3}H]-PtdIns-transfer activities of $Sec14^{V154F}$ and $Sec14^{V155F}$ were indifferent to NPPM and ergoline challenge under those conditions, as previously described (21, 22). Thus, the shallow himbacine pose accounts for why inhibition by this SMI is insensitive to the types of 'VV-motif' polymorphisms found in Sec14 PITPs of many virulent fungi.

Third, the signature of the medial region is engagement of SMIs with polar Sec14 sidechains (Fig. 3, *G–I*, 'medial' column). The precise subset differs for each SMI, but the primary interactions involve hydroxyl-containing amino acids (Ser, Thr, Tyr). The significance of these polar interactions is highlighted by Ser_{173} whose sidechain is involved in polar interactions with all SMIs and whose amide NH group forms a pocket-stabilizing H-bond with the carbonyl oxygen of Arg_{208} (Fig. 3*I*). Substitution of Ser_{173} to Cys is functionally nonconservative and results in essentially complete Sec14 resistance to the presently validated SMIs (20, 22).

Fourth, the distal SMI moieties (*e.g.* NPPM/NPBB B-rings, ergoline R2 group, and the himbacine D-ring) are positioned in a hydrophobic subregion of the collective SMI-binding envelope (Fig. 3, *J–L*, 'distal' column). This environment is lined primarily with methyl-containing sidechains and the aromatic ring of Phe_{212}.

In summary, the Sec14-directed SMIs of all four chemotypes exhibit binding modes that exploit a common amphiphilic substructure deep within the Sec14 lipid-binding cavity that hosts the natural ligands PtdCho and PtdIns, and offers chemical complementarity to diverse sets of SMIs.

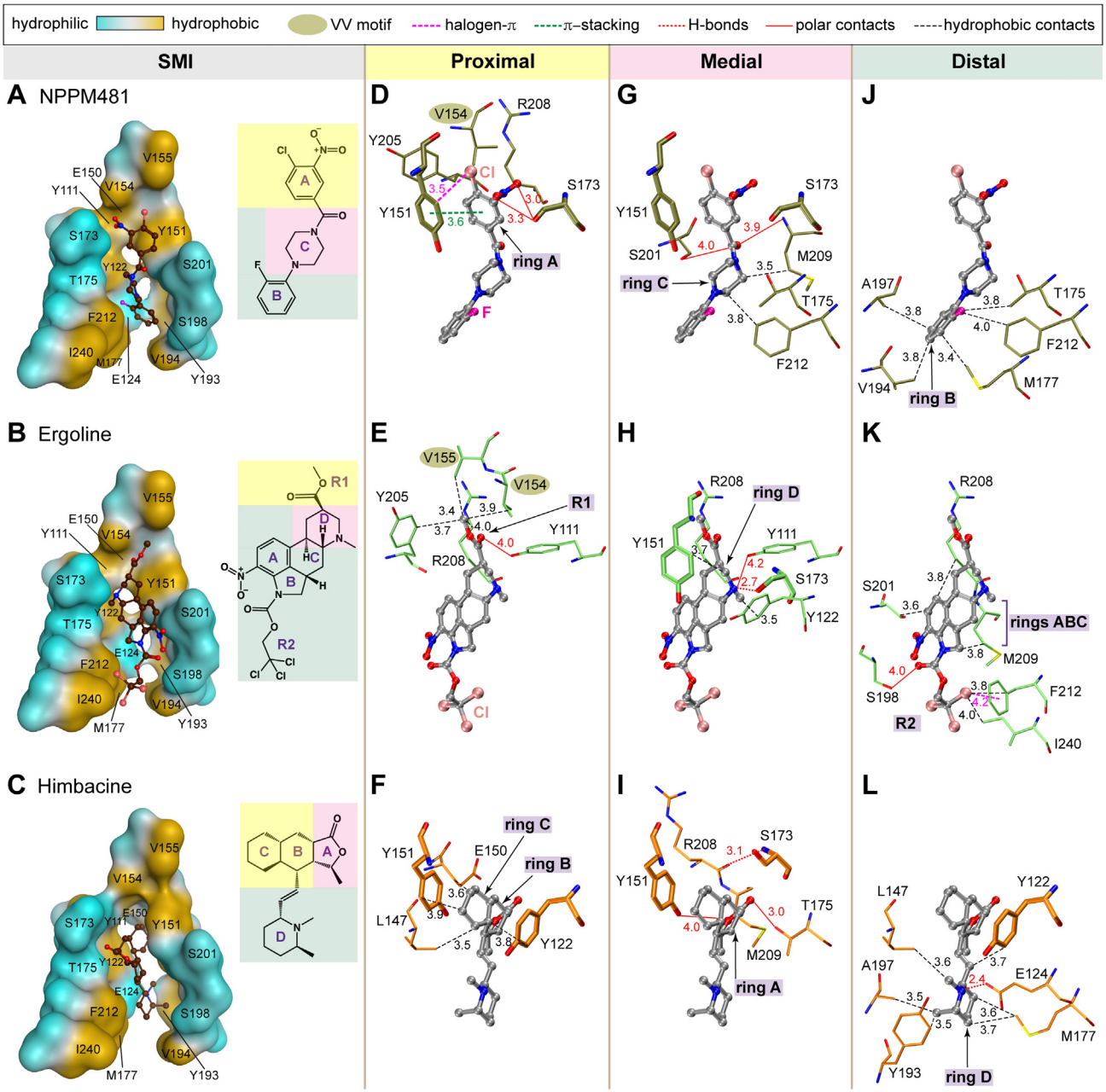

Figure 3. High resolution descriptions of SMI-binding modes. Poses of NPPM481, ergoline, and himbacine are shown in cut-away views of the common 21 amino acid–binding envelope (Panels *A–C*, respectively). Amino acids depicted in the cut-away are labeled. Tyr_{205}, Arg_{208}, and Met_{209} are omitted so as to not obstruct the view. Leu_{147} and Ala_{197} are not visible in this orientation. The envelope is rotated 90 degrees clockwise relative to its orientation in Figure 2. The chemical structures of the SMIs are presented in the same orientation as these appear in the panels of the corresponding rows. Panels *D*, *G*, and *J* depict the binding modes for the NPPM481 A-ring, C-ring and linker, and B-ring, respectively. In (*D*), Tyr_{111} is omitted to not obstruct the view of other interactions. The OH group of the Tyr_{111} sidechain forms a hydrogen bond with the nitro group of the NPPM481 A-ring. Panels *E*, *H*, and *K* detail Sec14 interactions with the ergoline carboxylic ester, fused ring system, and trichloroethyl-carboxylic ester constituents. Panels *F*, *I*, and *L* describe interactions between Sec14 and the himbacine *B* and *C* rings, the A-ring, and the D-ring, respectively. The intraprotein H-bond between Ser_{173} and Arg_{208} is shown in (*I*) to emphasize the polar character of the region. Atom color scheme: carbon (*gray*), oxygen (*red*), nitrogen (*dark blue*), chlorine (*pink*), and fluorine (*magenta*). Interaction key: halide-π interactions (*dashed magenta lines*), π-π interactions (*green dashed lines*), hydrophobic interactions (*dashed black lines*), polar interactions (*solid red lines*), and hydrogen bonds (*dashed red lines*). Corresponding distances are indicated in Å. SMI, small-molecule inhibitor.

^{19}F NMR spectroscopy provides a direct probe of SMI binding to Sec14

Dissection of mechanisms employed by the SMIs to invade the lipid-binding cavity of Sec14 requires direct atom-specific reporters of binding. The presence of the ^{19}F substituent in the NPPM481 B ring provides us with an opportunity to apply ^{19}F NMR spectroscopy to monitor the binding process. ^{19}F NMR spectroscopy has high sensitivity due to large gyromagnetic ratio of the ^{19}F nucleus and is free from protein background signals. To establish the validity of this approach, we applied it to the WT Sec14 and three other proteins whose common property is resistance to inhibition by NPPM481 *in vitro* and *in vivo*. These proteins are the Ser_{173}Cys and Val_{155}Phe variants of Sec14 and Sfh1*, a lipid exchange-activated mutant of the Sec14 paralog

Sfh1. As an NMR-compatible membrane mimic, we used isotropically tumbling DiC14:0 PtdCho (1,2-dimyristoyl-sn-glycero-3-phosphocholine, DMPC):Di C6:0 PtdCho (1,2-dihexanoyl-sn-glycero-3-phosphocholine, DHPC) bicelles (q = 0.5; 36) (Fig. 4*A*).

The ^{19}F NMR experiments were conducted in the "protein titration" mode where increasing amounts of Sec14 proteins were added to a solution containing 75 μM of NPPM481 preincubated with 80 mM bicelles (Fig. 4, *B–D*). In the protein-free solution, unbound NPPM481 gives rise to a single ^{19}F peak at −124.3 ppm. Upon increasing protein concentration, this peak decreases in intensity due to the formation of the protein::NPPM481 complex. The latter is evident from the appearance of a broad ^{19}F peak at ca. −(125.5–126.5) ppm.

Depletion of the unbound NPPM481 ^{19}F peak was used to extract the K_{eff} values (see Experimental procedures) and to quantify the effects of these mutations on Sec14–NPPM481 interactions (Fig. 4, *B–D*). The decrease in the effective binding affinities is 12-fold and 70-fold for the Val_{155}Phe and Ser_{173}Cys variants, respectively (Fig. 4*E*). We speculate that, in the case of the nonconservative Ser_{173}Cys substitution, the Ser-mediated interactions are altered by the lower electronegativity and/or larger atomic radius of sulfur, and differences in sidechain geometries (*i.e.*, bond lengths, Cβ-S-H angles) relative to Ser (37). Sfh1*, which has a native Phe residue at position 154 of the Sec14 'VV-motif' (29), failed to bind NPPM481 (inset of Fig. 4*C*). Thus, our data faithfully recapitulate the *in vitro* and *in vivo* results and are also in agreement with structural predictions regarding the role of (i) the VV-motif in accommodating the NPPM481 A-ring -and (ii) the contribution of Ser_{173} to the polar environment and stability of the lipid-binding pocket.

We further used ^{19}F NMR to evaluate the role of the A-ring halogen substituent in formation of the Sec14-SMI complexes. NPPM755 belongs to the same chemotype as NPPM481 but has a fluorine substituent in the A-ring instead of chlorine (Fig. 4*F*). This substitution renders NPPM755 an inactive Sec14 inhibitor *in vitro* and *in vivo* (20). The A- and B-ring fluorine atoms of NPPM755 give rise to distinct ^{19}F signals at -116.4 and -124.6 ppm, respectively. In the binary system containing equimolar Sec14 and NPPM755, both ^{19}F peaks broaden significantly due to the chemical exchange between unbound

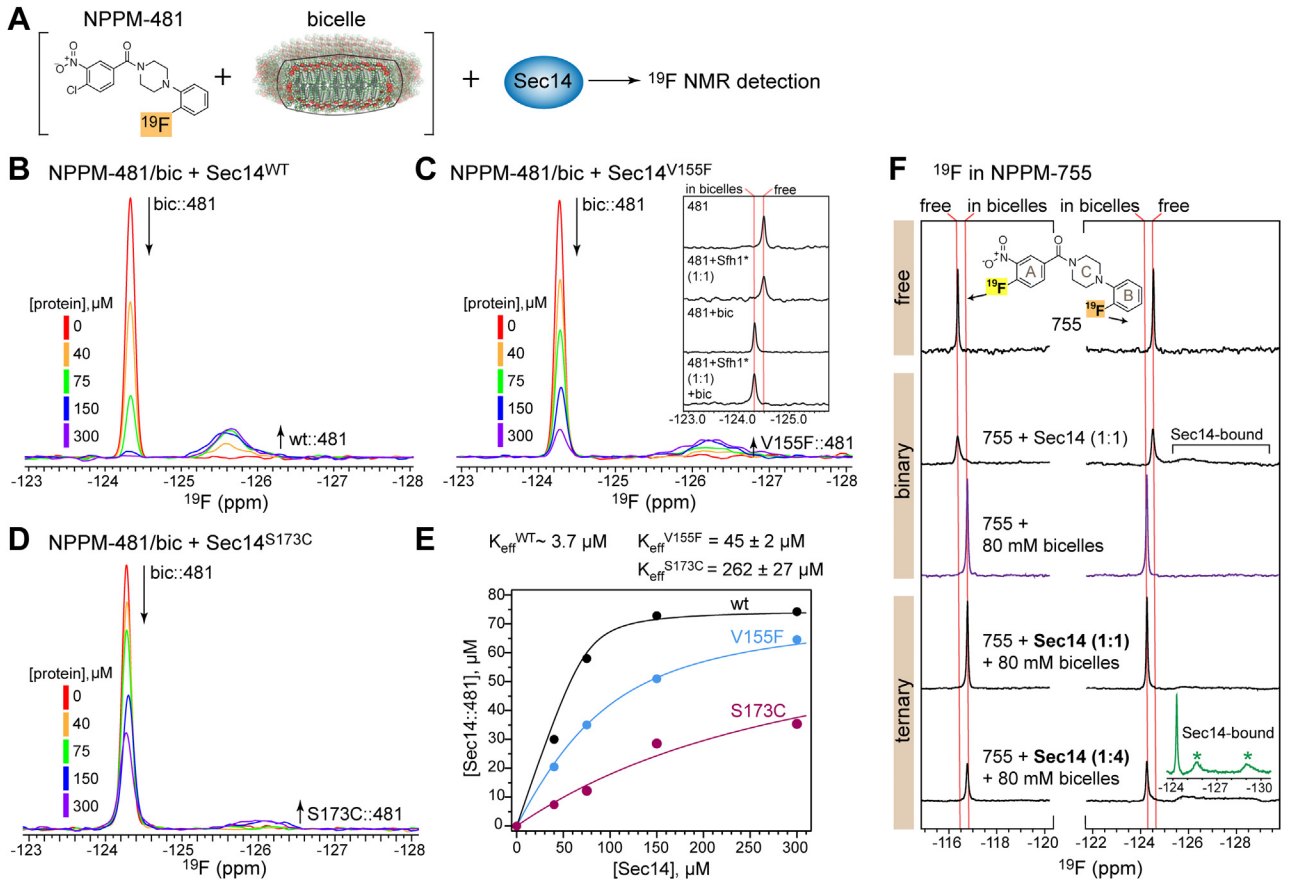

Figure 4. Quantification of NPPM binding to Sec14. *A*, schematic representation of ^{19}F NMR-detected binding experiments in an NPPM481-bicelle system in Sec14 titration mode. ^{19}F NMR spectra of 75 μM NPPM481 in bicelles as a function of the total concentration of Sec14 variants ranging from 0 to 300 μM: (*B*) WT, (*C*) Val_{155}Phe, and (*D*) Ser_{173}Cys. The inset of (*C*) shows the ^{19}F NMR spectra of 40 μM NPPM481 in solution, in presence of equimolar Sfh1*(Glu_{126}Ala), and in presence of DMPC/DHPC bicelles. *E*, the binding curves of NPPM481 to Sec14 WT and variants (Ser_{173}Cys and Val_{155}Phe) in the presence of DMPC/DHPC bicelles. The K_{eff} values for the Sec14 variants were obtained by fitting the curves as described in Experimental procedures. For Sec14, the K_{eff} value was estimated using the experiment of Figure 5*D*. *F*, ^{19}F NMR spectra of 75 μM NPPM755 in solution, in presence of equimolar Sec14, in presence of DMPC/DHPC bicelles, in presence of equimolar Sec14 and bicelles, and 4-fold excess of Sec14 and bicelles. The chemical structure of NPPM755 is depicted in the inset of top panel showing locations of the probes. Inset of the last panel shows the spectrum collected with the carrier at -126.8 ppm and the spectral width of 10 ppm. DHPC, 1,2-dihexanoyl-sn-glycero-3-phosphocholine.

and Sec14-bound species. The latter manifests itself as broad spectral features in the range of -(216–218) ppm.

As expected, NPPM755 quantitatively partitions into bicelles in a binary NPPM755/bicelle system as reported by the chemical shift changes of both ^{19}F peaks in those conditions (Fig. 4*F*, purple trace). The intensities of the ^{19}F peaks decreased upon addition of Sec14, indicating the formation of the Sec14::NPPM755 complex, with 8% and 63% protein-bound 755 at ligand-to-protein ratios of 1:1 and 1:4, respectively (Fig. 4*F*). This estimates K_{eff} to be in the range of ~200 μM, a value similar to the K_{eff} of Sec14^{S173C}–NPPM481 interactions. Despite the low affinity of NPPM755 binding, both ^{19}F signals originating from Sec14-bound NPPM755 were detected with appropriate adjustment (see Experimental procedures) of the NMR parameters (Fig. 4*F* inset, green spectra). The marked reduction in affinity can be explained by the inability of fluorine, due to its small atomic radius, to engage in edge-on halide-π interactions and to effectively interact with the hydrophobic pocket containing the VV-motif.

In summary, ^{19}F NMR-based detection of SMI binding to Sec14 provides a sensitive and direct method for quantifying SMI structure/activity relationship data and the effects of Sec14 mutations and naturally occurring polymorphisms.

NPPM481 displaces Sec14-complexed PtdCho at high lipid excess

^{19}F NMR detection was used to quantitatively evaluate the ability of NPPM481 to displace the native ligand PtdCho from Sec14 in the presence of membranes. To validate bicelles as a membrane mimic that supports Sec14 lipid-exchange activity, Sec14 was populated with fluorinated PtdCho (see Experimental procedures) and the fate of the lipid ^{19}F signal was followed upon addition of bicelles (Fig. 5*A*). The Sec14::^{19}F-PtdCho complex appears as a sharp peak at -216.4 ppm with a broader spectral feature at -219.0 ppm. Since Sec14-like PITPs favor a closed conformation when complexed to native lipid ligands (17, 28, 29, 34), we assigned the most intense peak at -216.4 ppm to the ^{19}F-PtdCho associated with the closed form of Sec14. The peak at -219 ppm likely corresponds to ^{19}F-PtdCho bound to the open form of Sec14. All Sec14-bound ^{19}F-PtdCho transferred to bicelles upon their addition to the protein-lipid complex, indicating that bicelles are suitable for investigating the inhibition of Sec14 lipid-exchange activity by NPPM481 using high-resolution NMR approaches. ^{19}F-PtdCho is more dynamic in bicelles than when bound to Sec14 as evidenced by the longer ^{19}F longitudinal relaxation time of bicelle-

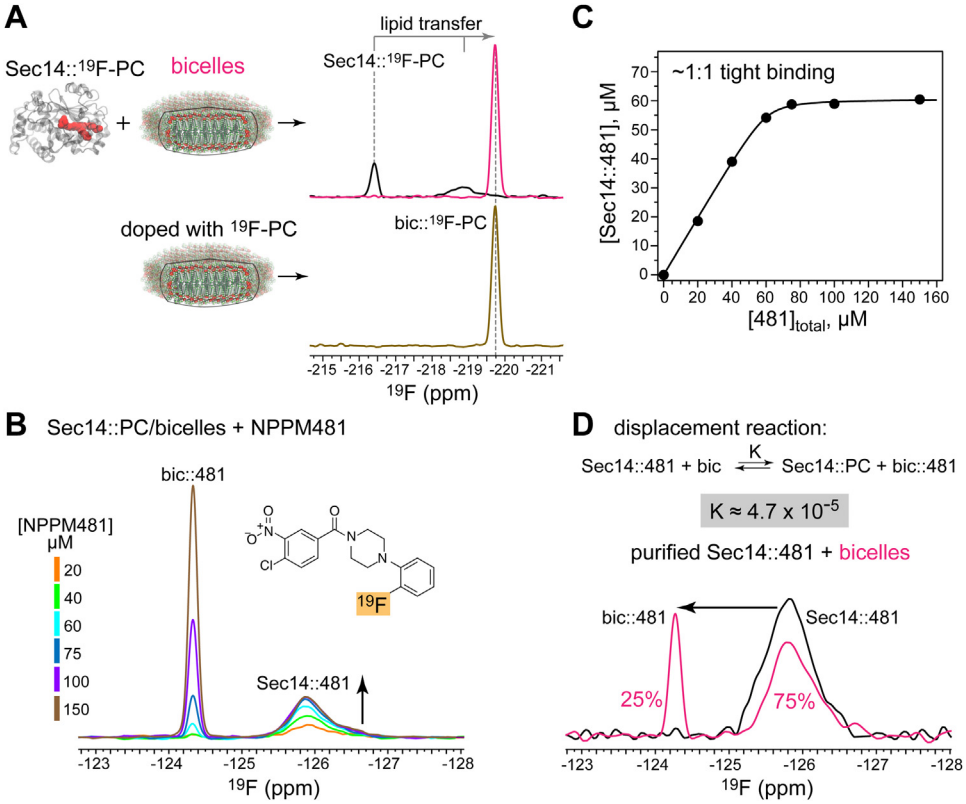

Figure 5. Membrane mimics facilitate Sec14 loading with NPPM481. NPPM481 and PtdCho labels are abbreviated to 481 and PC. *A*, top panel: ^{19}F NMR spectrum of the Sec14::^{19}F-PtdCho complex (*black*) undergoes drastic changes upon addition of DMPC/DHPC bicelles (*dark pink*). The appearance of a new peak at -219.7 ppm reports transfer of ^{19}F-PtdCho from Sec14 to bicelles. Bottom panel: the spectrum of ^{19}F-PtdCho incorporated into bicelles during preparation is shown for reference (tan). *B*, ^{19}F NMR-monitored titration of Sec14::PtdCho/bicelle system with NPPM481 (concentrations ranging from 0 to 150 μM). The buildup of the Sec14::NPPM481 complex is indicated with an *arrow*. *C*, the lipid-NPPM481 displacement curve plotted as a function of Sec14::NPPM481 concentration *versus* total NPPM481. The shape of the curve reports on high-affinity interactions of Sec14 with NPPM481 with full saturation attained under stoichiometric conditions. The *solid line* serves as visual guide. *D*, addition of bicelles to the purified Sec14::NPPM481 complex results in exchange of PtdCho for NPPM481– resulting in bic::NPPM481 and Sec14::NPPM481 populations of 25% and 75%, respectively. The estimated K value for the displacement reaction is 4.7 × 10^{-5}. The total concentration of Sec14 is 45 μM. DHPC, 1,2-dihexanoyl-sn-glycero-3-phosphocholine; PtdCho, phosphatidylcholine.

incorporated lipid (T_1 =1.4 s) compared to Sec14-bound lipid (T_1 = 0.8 s) (Fig. S4*A*).

^{19}F NMR-monitored NPPM481-binding experiments were conducted by titrating NPPM481 into a system where Sec14::PtdCho was preincubated with 80 mM bicelles (Fig. 5*B*). The free and Sec14-bound NPPM481 pools manifest themselves as narrow and broad ^{19}F peaks at -124.3 and -125.9 ppm, respectively. The peak areas were used to calculate the concentration of the Sec14::NPPM481 complex and construct a lipid-NPPM481 displacement curve (Fig. 5*C*). Saturation is reached at an ∼1:1 ratio of Sec14 to NPPM481, reporting a high-affinity interaction. The tight binding regime precluded reliable determination of the equilibrium constant from these data. We therefore took advantage of the high-affinity interactions between Sec14 and NPPM481 to purify the Sec14::NPPM481 complex. Addition of bicelles to the complex resulted in the transfer of 25% of bound NPPM481 from Sec14 to bicelles (Fig. 5*D*). Quantification of the ^{19}F peak areas allowed us to estimate the effective dissociation constant of the Sec14::NPPM481 complex $K_{eff} = K[bic]_t$, where K is the equilibrium constant for the exchange reaction and $[bic]_t$ is the total concentration of lipids in bicelles (see Experimental procedures). The K_{eff} and K values are 3.7 μM and $4.7 \cdot 10^{-5}$, respectively. These values indicate that formation of the Sec14::NPPM481 complex is thermodynamically strongly favored (ΔG^o = −24.7 kJ/mole) and occurs even when the natural Sec14 ligand PtdCho is in ∼2000-fold molar excess.

In all bicelle-containing experiments, the ^{19}F peak of free (*i.e.*, not Sec14-bound) NPPM481 was shifted ∼0.3 ppm downfield compared to its value in solution. Control experiments established that this shift reports on the partitioning of NPPM481 into bicelles (Fig. S4*B*). This observation is consistent with the NPPM481 $C_{log}P$ value of 2.7 that predicts that for every NPPM481 molecule free in solution there are ∼500 membrane-incorporated molecules. If SMIs inhibit Sec14 by incorporating into the lipid-binding cavity from a membrane environment during the lipid-exchange cycle, as previously suggested (20), what are the implications for the geometry of Sec14–membrane interactions?

NPPM481 partitions into the hydrocarbon region of membranes

As Sec14 is a peripheral membrane protein proposed to bind SMI at the membrane interface (20), it was of interest to assess the insertion depth and orientation of NPPM481 in the membrane as probe for how Sec14 might engage the SMI in a membrane environment. To that end, atomistic MD simulations of binary systems comprising NPPM481 and Di14:0 PtdCho (DMPC) bilayers were conducted. DMPC was employed as bulk lipid in the simulations to match experimental conditions. To enable these simulations, we developed a CHARMM-compatible force field for NPPM481 (Figs. S5, and S6; see Experimental procedures).

To eliminate bias, four systems with different initial conditions were prepared and subjected to 500 ns production runs. In system 1, one NPPM481 molecule was placed in solution 20 Å above the bilayer, and the simulations were conducted twice. In systems 2, 3, and 4, 16 NPPM481 molecules were pre-inserted into the membrane at the bilayer center (system 2), the hydrocarbon region (system 3, eight molecules per leaflet), and the headgroup region (system 4, eight molecules per leaflet). In system 1, the NPPM481 molecule spontaneously partitioned into the bilayer at 47 ns/142 ns and remained there for the entire duration of the production run (Figs. 6*A* and S7*A*). In systems 2 to 4, the membrane-initialized NPPM481 molecules redistributed within the bilayer and equilibrated within ∼100 ns (Fig. S7*B*). Thus, the last 400 ns of all trajectories were used for subsequent analyses.

Irrespective of the initial conditions, NPPM481 molecules converge to the same position in the membrane as evidenced by the similarities of all mass density profiles along the membrane normal (Figs. 6*B* and S7*C*). The molecules partition into the hydrocarbon region of the bilayer with NPPM481 positioned ∼9 Å above the bilayer center and ∼9 Å below the headgroup region. The membrane densities of the halogen atoms (A-ring Cl, B-ring F) report slightly deeper insertion with the corresponding peaks centered at ∼8 Å above the bilayer center in both cases.

To assess the orientation preferences of the NPPM481 A-ring in the membrane, we defined a vector that lies in the plane of the A-ring and connects the carbonyl carbon and the Cl atom of NPPM481. Angle θ between this vector and the membrane normal describes the orientation of the A-ring in the membrane (Fig. 6*C*). Representative heat maps for Systems 1 and 3, where θ is plotted against the distance between the A-ring geometric center and the bilayer center, reveal a consistent pattern (Fig. 6*C*). Angle θ is centered at 76° (corresponding to a near-parallel A-ring vector orientation relative to the membrane surface), with an SD of ∼30°. The distributions are modestly skewed in that smaller tilt angles correlate with deeper membrane insertion of the A-ring and vice versa. The A-ring center is positioned at ∼9 Å away from the bilayer center and 11 to 12 Å below the lipid-water interface with the closest approach to the interface of ∼6 Å. That is, a position where the ring center and its Cl substituent reside at the level of ester moieties of the headgroup region.

In summary, the MD data on the NPPM481-bicelle system project an unexpectedly deep pose for NPPM481 in the bilayer environment. For the Sec14 lipid-binding pocket to capture NPPM481, the protein must either penetrate deep into the bilayer or introduce local membrane perturbations that raise NPPM481 closer to the membrane surface.

Sec14 binding by aqueous NPPM481 displaces PtdCho from its binding site

The current view is that Sec14 (and PITPs in general) shield the lipid-binding cavity from solvent when in solution and that this cavity is largely inaccessible to solvated small molecules under those conditions (28). We set out to interrogate this

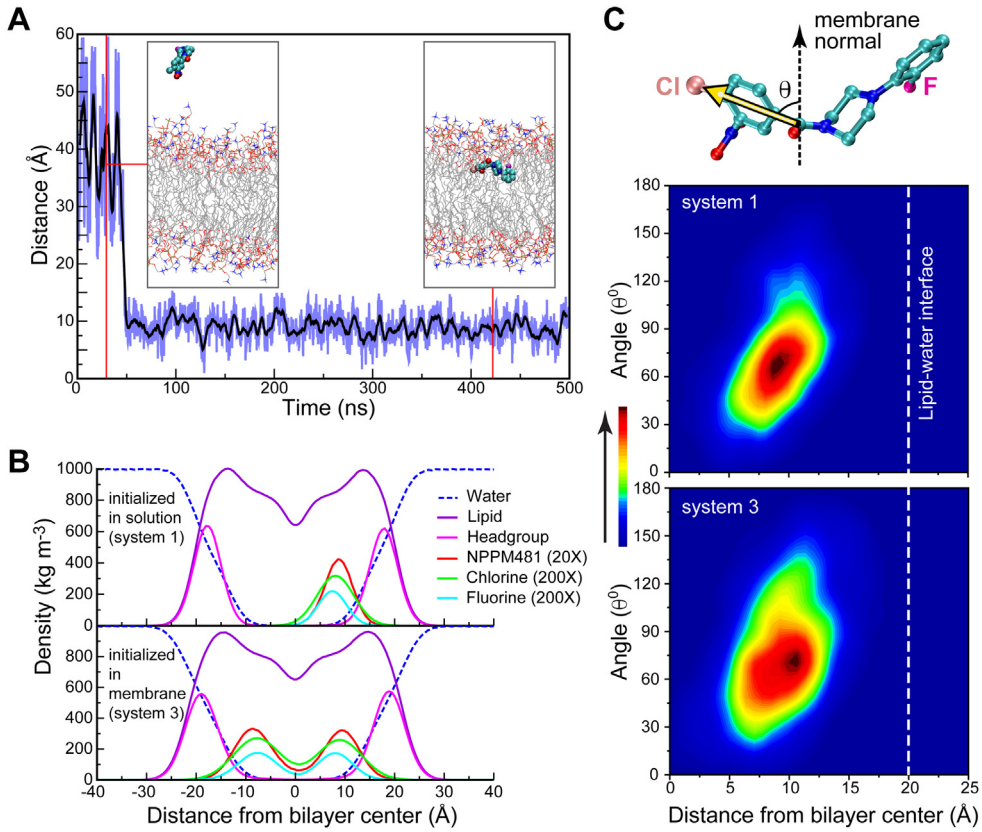

Figure 6. NPPM481 spontaneously partitions into the acyl chain region of membrane bilayers. *A*, distance along the Z axis (parallel to the membrane normal) between the NPPM481 center-of-mass and center of the membrane plotted along the 0.5 μs trajectory. The system was initialized with the NPPM481 molecule placed in solution 20 Å above the bilayer. Spontaneous partitioning into the membrane occurred at 47 ns and persisted throughout the production run. *B*, mass density profiles were calculated for NPPM481 initialized in solution (*top graph*) and in the hydrocarbon region of membranes (*bottom graph*). Irrespective of initial conditions, NPPM481 molecules and their Cl and F substituents converge to the same position when projected onto the membrane normal. *C*, heat maps correlating the distance between the NPPM481 A-ring and the bilayer center, and the A-ring tilt angle. The tilt angle is defined as the angle between the vector connecting the carbonyl carbon and the Cl atom of NPPM481, and the membrane normal. Irrespective of initial conditions, the A-ring center is positioned ∼11 to 12 Å below the lipid-water interface, and the tilt angle is centered at ∼76°.

notion in a binary membrane-free system consisting of Sec14::^{19}F-PtdCho and NPPM481 (Fig. 7*A*). ^{19}F NMR spectra were collected for two spectral regions. One was centered at −216 ppm to monitor ^{19}F-PtdCho (Fig. 7*B*), and the second was centered at −123 ppm to monitor NPPM481 (Fig. 7*C*).

Addition of progressively increasing amounts of NPPM481 to Sec14::^{19}F-PtdCho in the membrane-free system resulted in drastic changes in both NMR spectra. Specifically, the ^{19}F-PtdCho peak at -216.4 ppm decreases in intensity upon titration with NPPM481, indicating that ^{19}F-PtdCho is being displaced from its position within the Sec14 pocket (Fig. 7*B*). This is accompanied by enhancement of the broad ^{19}F spectral features in the −217.5 to −219.5 ppm range that we assign to the displaced ^{19}F-PtdCho. Since no membrane environment was present, the lipid likely remains associated with the host Sec14 molecule. The fact that ^{19}F-PtdCho is indeed displaced by NPPM481 from its resident binding site in Sec14 is further corroborated by the increase in the intensity of the ^{19}F peak at −125.9 ppm that corresponds to the Sec14::NPPM481 complex (Fig. 7*C*). The ^{19}F signal originating from the complex is easily distinguishable from that of free NPPM481 (−124.5 ppm), due to the broader linewidth of the former associated with the increase in rotational correlation time.

Quantitative analysis of the ^{19}F NMR spectra produced fractional populations of Sec14 species with the lipid-binding cavity occupied by ^{19}F-PtdCho ($f_{Sec14::PC}$) and NPPM481 ($f_{Sec14::481}$). The plot of those values as a function of total NPPM481 concentration shows gradual redistribution between these two species with increasing NPPM481 concentration (Fig. 7*D*). Moreover, the sum of the fractional populations is ∼1 for all points. This feature indicates that the quantitative analyses, conducted independently for the two spectral regions (see Experimental procedures), are internally self-consistent. Half-saturation of Sec14 with NPPM481 is achieved at a stoichiometry of ∼0.7 SMI:1.0 Sec14. Collectively, these data suggest the Sec14 lipid-binding cavity is accessible to NPPM481 in an aqueous membrane-free system, and that PtdCho displacement by NPPM481 results in the formation of the ternary complex where the lipid remains associated with SMI-bound protein.

To determine if the preformed ternary complex can complete a lipid-exchange cycle upon interaction with membranes, bicelles were added to the binary system containing 2-fold excess of NPPM481 relative to Sec14::^{19}F-PtdCho with the respective concentrations set at 150 μM and 75 μM. Note that only partial displacement of ^{19}F-PtdCho from the Sec14 lipid-binding pocket

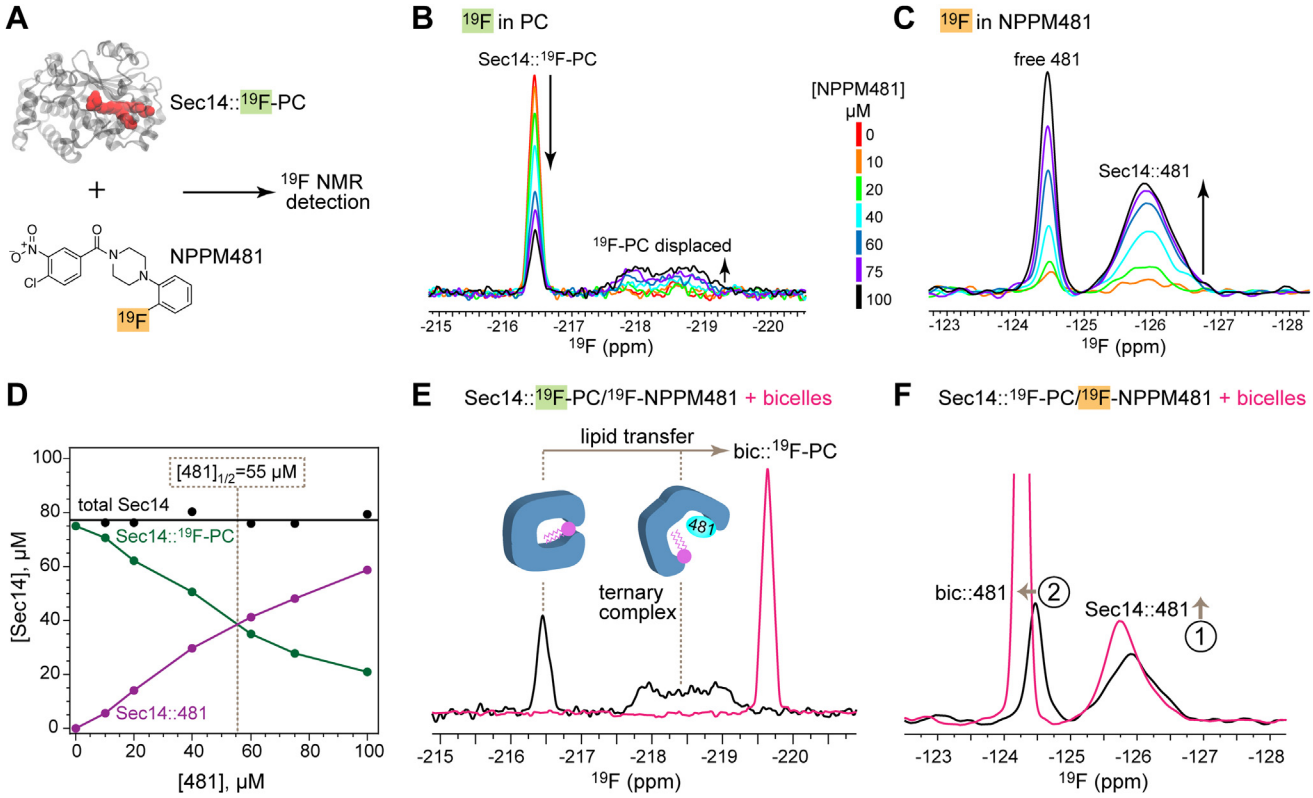

Figure 7. NPPM481 loads into Sec14 directly from solution. *A*, schematic representation of ^{19}F NMR-detected binding experiments in the binary Sec14::^{19}F-PtdCho-NPPM481 system. Sec14-bound ^{19}F-PtdCho is shown in *red*. ^{19}F NMR spectra showing response of the ^{19}F signals in ^{19}F-PtdCho (*B*) and NPPM481 (*C*) as a function of total NPPM481 concentration ranging from 0 to 100 μM. The total Sec14::PtdCho concentration was 75 μM. *D*, redistribution of PtdCho- (*red*) and NPPM481-complexed Sec14 (*blue*) upon increasing the total NPPM481 concentration. The data were obtained from quantitative analysis of the ^{19}F NMR spectra as described in Experimental procedures. Sec14 half-saturation is reached at a Sec14:NPPM481 ratio of 1:0.73 (*i.e.* 55 μM NPPM481). *E*, addition of bicelles to Sec14::^{19}F-PtdCho and NPPM481 (Sec14::^{19}F-PtdCho:NPPM481 M ratio = 1:2) results in a complete transfer of the ^{19}F-PtdCho from Sec14 to bicelles, and (*F*) the 25% increase in the concentration of the Sec14::NPPM481 complex (1), and partitioning of free NPPM481 into bicelles (2). We interpret the high intensity of the ^{19}F bic::NPPM481 peak to reflect solubilization of NPPM481 aggregates (not detectable by NMR due to their high molecular mass) by bicelles. PtdCho, phosphatidylcholine.

by NPPM481 is achieved under these conditions because NPPM481 reaches its solubility limit at ∼120 to 150 μM and is no longer accessible to Sec14 at higher concentrations, likely due to the formation of colloidal aggregates. We find that both the ^{19}F-PtdCho fraction remaining in the Sec14 pocket, and the fraction displaced by NPPM481, are transferred to bicelles (Fig. 7*E*). The presence of membranes also results in an ∼25% increase in the concentration of the Sec14::NPPM481 complex and partitioning of the aqueous unbound NPPM481 into the bicelles (Fig. 7*F*).

In summary, these findings indicate that NPPM481 can access the Sec14 lipid-binding pocket in membrane-free systems, and that this pathway of inhibition results in formation of a ternary Sec14::NPPM481::PtdCho complex that is competent with respect to the terminal steps of lipid-exchange. Efficient solubilization of NPPM481 by membranes is accompanied by the increase in the population of the Sec14::NPPM481 complex.

Sec14 dynamics and solvent accessibility of the lipid-binding cavity

The ability of NPPM481 to invade the Sec14 lipid-binding pocket in the membrane-free system suggests that Sec14 undergoes conformational transitions that are not obligatorily triggered by its membrane encounters (Fig. 1*A*). Little is known about these transitions as the only available data to this effect come from very short (32 ns) MD simulations that employed an open and artificially constructed apo-Sec14 conformer as starting structure (17, 34). To probe the dynamic behavior of the ligand-complexed Sec14, 2 μs atomistic MD simulations were conducted with the Sec14::NPPM481 complex as starting configuration.

Backbone RMSF analysis revealed a rich dynamic profile for Sec14. The dynamic elements with elevated RMSF values include helices α6-α10, the N-terminal segment of the G-module (a conformational switch element; (32), the 3_{10} helix T6, α5, and the loop that connects helices α4 and α5 ($L_{4/5}$) (Fig. S8*A*). The spatial fluctuations between these elements are apparent in the contact map that correlates the SDs of inter-residue distances (Fig. S8*B*). When viewed in the context of the 3D protein structure, the dynamic regions of Sec14 form a discrete structural element composed primarily of helical and loop regions (Fig. S8*C*). We specifically highlight the Sec14 conformational transition that modulates solvent access to the lipid-binding pocket. The drastic nature and large scale of this transition is evident in the RMSD plots of both independent

1 μs trajectories (Figs. 8*A* and S9*A*). The major contributor is the repositioning of two helical elements, α9 and α10 (the latter previously defined as the "gate" element; (17, 28, 32)) that closes the lipid-binding pocket. In the "open" Sec14 conformer, which is represented in all Sec14 crystal structures determined to date and in our starting configuration (28, 29), the α9/α10 helices are >20 Å apart as measured by the distance between the Cα carbons of the α9 and α10 residues Arg_{195} and Phe_{231}, respectively. During the course of the simulations, the α9/α10 distance is reduced to ∼8 Å, and the two helices form an interface that closes the lipid-binding pocket. The relatively immobile segment of α8 provides a reference point for measuring the movements of both helices (Figs. 8*B* and S9*B*).

Cluster analyses of the combined trajectories identified four major clusters that cover 96% of the structures (Figs. 8*C* and

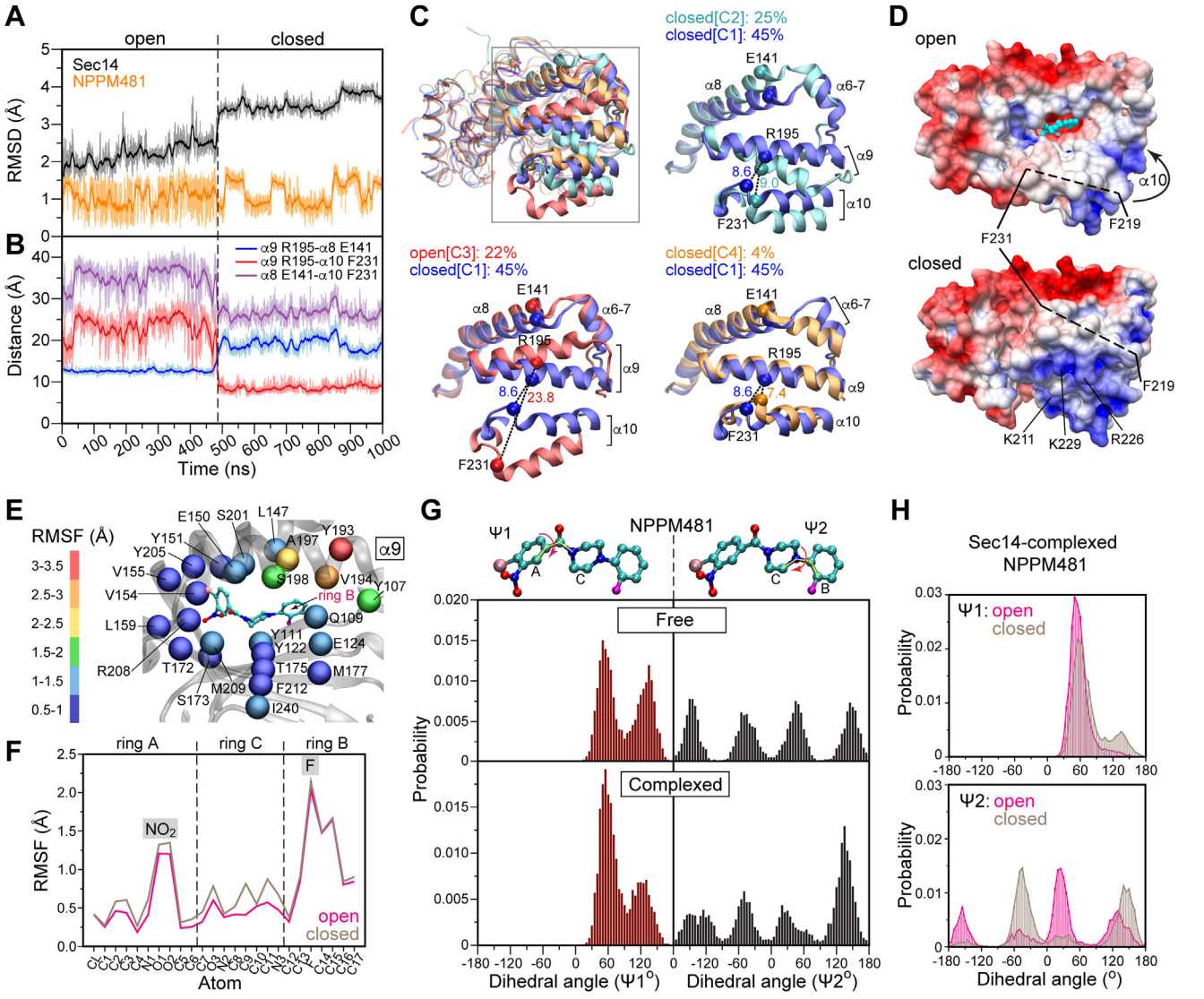

Figure 8. Dynamics of the Sec14::NPPM481 complex. *A*, RMSD values of the Sec14 backbone (*black*) and NPPM481 (all heavy atoms, *orange*) plotted along the 1 μs trajectory. The open-to-closed transition at 487 ns is indicated with a *vertical dashed line*. *B*, "Ruler" distances between the helices α8-α9 (*blue*), α9-α10 (*red*), and α8-α10 (*purple*) are shown. Open-to-closed transition of Sec14 involves formation of the α9-α10 helix-helix interface. *C*, full and pairwise overlay of representative Sec14::NPPM481 cluster structures illustrating structural variability of the helical segments α6-α10. The clusters are labeled C1 through C4. C1, C2, and C4 correspond to closed conformations, while C3 corresponds to an open conformation. *D*, electrostatic potential mapped onto the representative cluster structures of the open and closed Sec14::NPPM481. The axis of the α10 segment bounded by residues 219-231 is shown with a *dashed line*. Realignment of the helical segments increases the hydrophilicity of the Sec14 surface through sequestration of the α10 hydrophobic face in helix-helix contacts with α9, and the positioning of an extensive positively charged patch over the ligand-binding site. *E*, backbone RMSF values of the Sec14 residues that line the lipid-binding pocket. The RMSF values are color-coded and mapped onto the corresponding Cα atoms. There exists a gradient of flexibility along the lipid-binding pocket with most dynamic residues residing on α9. *F*, per-atom RMSF values of the Sec14-bound NPPM481. The most dynamic segments are the nitro-group of the A-ring and the entire B-ring that undergoes rotameric flips. The ligand dynamics are similar in the open and closed conformations of the complex. *G*, distributions of the dihedral angles Ψ1 (*brown bars*) and Ψ2 (*black bars*) that describe the relative orientations of rings A/C and C/B, respectively. The histograms were generated using 0.5 μs free NPPM481 and 2 μs (combined) Sec14::NPPM481 production runs. Comparison of the Ψ1 and Ψ2 distributions between the free (*top panel*) and Sec14-bound NPPM481 (*bottom panel*) shows that the ligand, especially the B-ring, retains considerable rotameric flexibility upon Sec14 binding. *H*, histograms of dihedral angles calculated using 1 μs trajectory of (A) and separated according to the open/closed states of the Sec14::NPPM481 complex. Transition to the closed state restricts the relative orientation of the C/B rings to two preferred values, Ψ2 ∼ −45° and ∼150°. The Ψ1 distribution is not significantly affected by transition to the closed state.

S9*C*). Only one cluster (C3, 22%) describes an open Sec14 conformer, whereas the other three describe closed Sec14 conformers (C1, 45%; C2, 25%; C4, 4%). These three clusters differ in the relative position of the α9/α10 helical pair and the α6-7 segment but preserve the closed α9/α10 interface as reported by the interhelical distances of 7 to 9 Å (Fig. 8*C*). The differences in the surface properties of the open and closed conformations are drastic (Fig. 8*D*). In the open conformation, the Sec14 ligand-binding site is accessible and a large hydrophobic region is solvent exposed. Sec14 surface hydrophilicity increases significantly upon α10 "gate" closure as the α10 hydrophobic ridge is sequestered by formation of α9-α10 interhelical contacts that position a positively charged patch over the cavity opening (Fig. 8*D*). These data support the idea that the closed Sec14 conformer dominates in solution as suggested previously (17, 28, 30, 34).

How do these large conformational rearrangements affect the dynamics of bound SMI? Of all residues that line the ligand-binding pocket, only five score as highly dynamic (RMSF values >1.5 Å). Color-coding of the residues according to the RMSF values illustrates the dynamic "gradient" across the ligand-binding pocket (Fig. 8*E*). Bound NPPM481 mirrors this pattern. Other than the -NO_2 substituent, the A-ring shows low RMSF values as it is tightly anchored to the Sec14 VV-motif pocket (Figs. 8*F* and S8*D*). By contrast, the NPPM481 B-ring is positioned near the mobile C-terminal segment of helix α9 and the B-ring atoms show high RMSF values (Fig. 8*F*). Closure of the ligand-binding site brings α9 in proximity to the B-ring, as reported by the reduced distances between the B-ring apex (marked by C-16) and the sidechains of Ala_{197} and Tyr_{193} (Fig. S8*D*).

The rotameric flexibility of bound NPPM481 was assessed by examining the distributions of the two dihedral angles that report on the relative orientations of the A/C and C/B rings (ψ1 and ψ2, respectively). While the ranges of sampled ψ1 and ψ2 values were similar between the free and Sec14-bound NPPM481 states, the latter form showed clear preferences for ψ1 ∼ 60° and ψ2 ∼ 140° (Fig. 8*G*). When the ψ1 and ψ2 distributions were independently analyzed for the open and closed Sec14::NPPM481 conformers, the data report that conformational transition to the closed state restricted the range of ψ2 by ∼100° and shifted the most frequently sampled ψ2 state from 25° to −45° (Fig. 8*H*). This restriction of NPPM481 rotameric states is also evident in RMSD traces where the SMI adopted a more limited set of discrete states in the closed conformer relative to the open conformer (Figs. 8*A* and S9*A*).

In summary, MD simulations of the Sec14::NPPM481 complex describe the conformational transitions that modulate solvent accessibility of the Sec14 lipid-binding pocket in atomistic detail. Together with the results on the membrane-free system (Fig. 7), these data suggest Sec14 samples both closed and open conformations in solution. While the majority of Sec14 residues lining the lipid-binding site do not show significant dynamics, the large volume of the binding cavity permits significant SMI flexibility, as exemplified by the motions of the NPPM481 B-ring. This feature of the Sec14-bound state likely makes favorable entropic contributions to the thermodynamics of the NPPM481-PtdCho displacement reaction.

Discussion

The roles of PITPs in regulating cellular lipid signaling and homeostasis represent an intense focus of interest in contemporary cell biology. Yet, the protein and lipid dynamics that underlie the lipid exchange cycle, and are central to potentiation of PtdIns 4-OH kinase signaling, remain essentially unstudied. Herein, we take advantage of Sec14-directed SMIs and an integrative structural approach to: (i) determine how chemically diverse SMIs arrest Sec14-mediated lipid exchange, (ii) outline pathways for how SMIs engage Sec14 in high affinity interactions, and (iii) glean new insights into the mechanics of the PITP lipid exchange cycle. Our results demonstrate that Sec14 can be inhibited by both membrane-incorporated SMI and SMI pools that exist in solution. These processes are enabled by the unexpectedly rich dynamic behavior of Sec14 substructures that gate the lipid-binding pocket. The data further project that Sec14 inserts deeply into the cytosolic leaflet of a membrane during the lipid exchange process. These collective results not only demonstrate the utility of Sec14-directed SMIs for biochemical dissection of the Sec14 lipid-exchange cycle but also outline new ideas regarding the development of novel classes of antifungal drugs, an area of intense interest in the contemporary infectious disease arena.

Chemical versatility of the Sec14 lipid-binding cavity for SMI binding

SMIs of all four chemotypes analyzed herein adopt poses deep within the Sec14 lipid-binding cavity in a common amphiphilic envelope dedicated to differential binding of both of its natural ligands, PtdCho and PtdIns. The ability of SMIs of diverse chemotypes to be accommodated in this common envelope, when coupled with the modest conformational changes that accompany binding of SMIs of different chemotypes, highlights the rich chemical complementarity available in this environment for the accommodation of diverse sets of small molecules. This complementarity is revealed when Sec14 is permitted to explore an expansive chemical space — that is, one larger than the one offered by its native cellular environment where Sec14 binds PtdIns and PtdCho specifically.

The versatility of the Sec14 lipid-binding cavity in binding SMIs primarily rests with the sidechains of residues that line the cavity and provide multiple options for polar and nonpolar interactions. Tyrosines are especially notable in this regard due to the impressive range of interactions these form with SMIs. These include H-bonding, ring stacking, methyl-π, and 'edge-on' halide-π interactions. As versatile as this chemical environment is, it is one that supports exquisitely tuned Sec14-SMI interactions. Residue Ser_{173} highlights this point. A seemingly subtle Ser_{173}Cys substitution is functionally nonconservative in this context as it strongly abrogates SMI binding and results

in essentially complete Sec14 resistance to the presently validated SMIs.

Our structural studies further indicate this chemical versatility presents *ab initio* docking approaches with serious challenges. This point is emphasized by comparisons of published Sec14::NPPM481 and Sec14::ergoline dock models with the respective crystal structures (Fig. 9*A*; (20, 33)). In both cases, the dock poses depart significantly from the direct experimental results reported herein. While the docking routines employed to arrive at these models were exhaustive and restrained the SMI sampling space to the Sec14 lipid-binding cavity, these approaches nonetheless produced model poses that fail to identify interactions crucial for high-affinity SMI binding. In particular, critical NPPM and ergoline interactions with Sec14 residues that line the hydrophobic VV-motif pocket are missed as the SMIs are mispositioned in shallower regions of the Sec14 lipid-binding cavity in both cases (Fig. 9*A*).

We conclude that the impressive potential for chemical complementarity offered by this amphiphilic region of the Sec14 lipid-binding cavity, in conjunction with the spacious volume (~3000 Å^3) and surface area of this cavity, offers multiple energetically favorable possibilities for docking solutions. This difficulty is potentially further exacerbated by subtle alterations in lipid-binding cavity geometry in crystal structures as a result of crystal packing. Either way, both

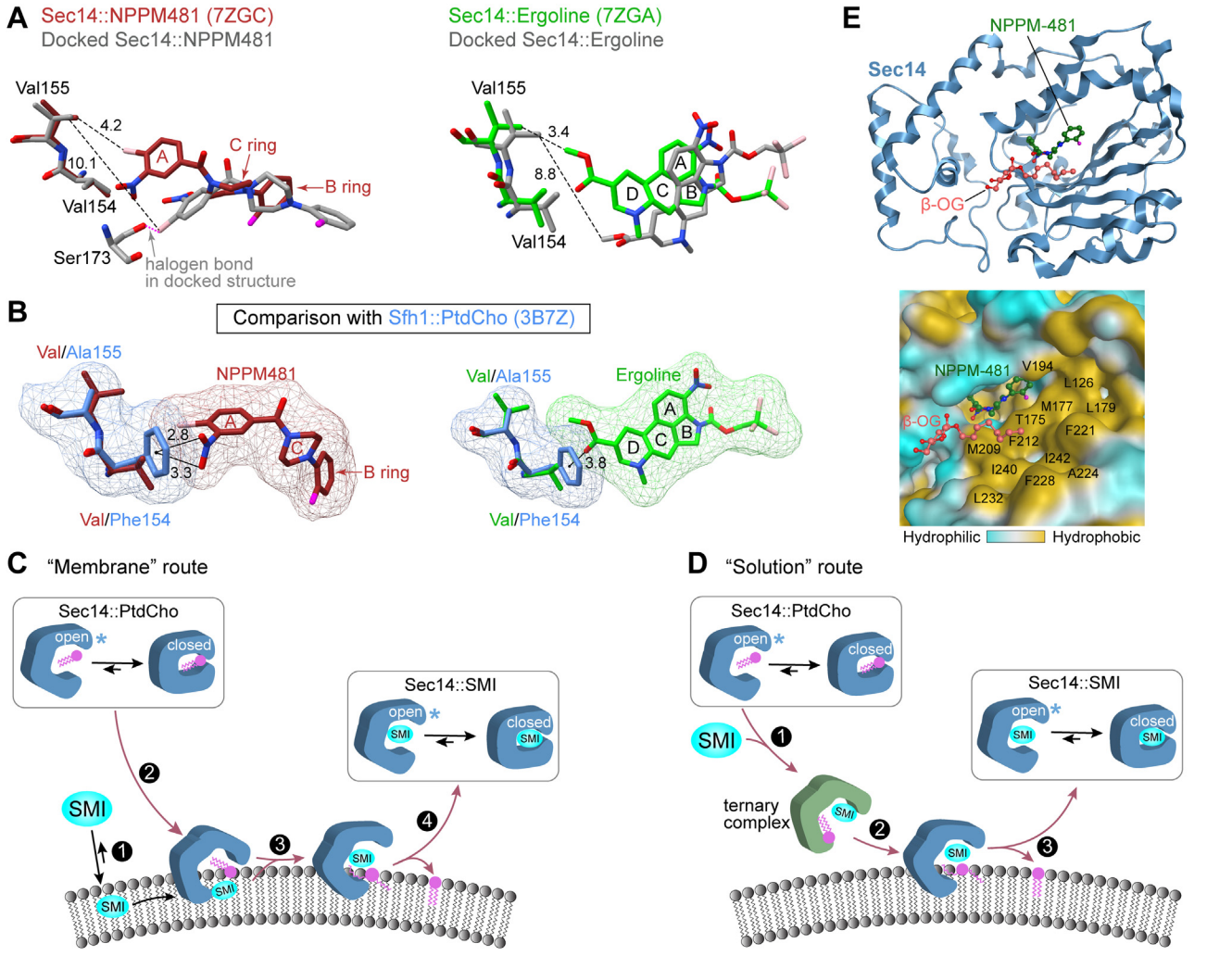

Figure 9. Pathways for Sec14 inhibition by small-molecule inhibitors. *A*, crystal structures of Sec14::NPPM481 and Sec14:ergoline (PDB entries 7ZGC and 7ZGA, respectively) are compared with the corresponding docked structures reported by Nile *et al* (2014) and Fillipuzi *et al* (2016), respectively. Backbone atoms in the crystal structures and docked structures are superposed. The VV-motifs are shown for reference. *B*, the backbone atoms of Sec14::NPPM481 and Sec14::ergoline are superposed onto the Sfh1::PtdCho structure (PDB entry 3B7Z), as indicated. Sfh1 exhibits a Phe_{154} Ala_{155} polymorphism in the VV-motif. *C*, membrane route for Sec14 inhibition by NPPM481 (SMI) in the course of a canonical lipid exchange reaction cycle is illustrated. *Asterisk* indicates open Sec14 conformers in solution might differ from those formed on membrane surfaces. *D*, solution route by which NPPM481 invades the Sec14 lipid-binding cavity and displaces the resident PtdCho molecule from its natural binding site is illustrated. A Sec14::NPPM481::PtdCho ternary complex is formed that, upon addition of membranes, resolves into an SMI-bound Sec14 complex with PtdCho released into the bilayer environment. *Asterisk* indicates open Sec14 conformers in solution might differ from those formed on membrane surfaces. *E*, potential binding site in the ternary complex for accommodating the PtdCho molecule displaced by NPPM481 *via* the solution inhibition route. In the crystal structure of the open Sec14 conformer (PDB entry, 1AUA), two molecules of octyl-β-glucopyranoside occupy the lipid-binding cavity. One overlaps the NPPM481-binding site (not shown), but the other resides in a hydrophobic environment of the lipid-binding cavity that is exposed in the open conformer and is an attractive candidate for displaced PtdCho binding. PtdCho, phosphatidylcholine; SMI, small-molecule inhibitor.

NPPM481 and ergoline dock models identified a number of SMI-interacting residues accurately, yet misidentified the precise Sec14-SMI interactions. For example, the favored NPPM481 dock pose predicted a halogen bond between the A-ring chlorine and Ser_{173} — a prediction supported by chemical structure/activity relationship, genetic, and biochemical data (20). Yet, the Sec14::NPPM crystal structures provide no evidence for halogen-bond interactions of NPPM481 or NPPM244 with Ser_{173}. Rather, these structures identify 'edge-on' halide-π interactions of the NPPM A-ring halide with Tyr_{151} — a residue that lines the VV-motif pocket and makes essential contributions to high affinity Sec14–NPPM and Sec14–ergoline interactions.

Insights into rational design of next-generation anti-mycotics

There is at present considerable urgency surrounding development of next-generation pharmaceuticals given the emergence of fungal 'superbugs' resistant to the limited set of anti-mycotics used in clinical settings (38–40). Sensitivity of a fungal Sec14 to validated SMIs is predicted by (i) the set of Sec14 residues involved in coordinating PtdCho headgroup-binding (*i.e.*, the PtdCho-binding barcode (20) and (ii) the $Val_{154}Val_{155}$ (VV)-motif (21, 25, 26). Most virulent fungi express Sec14 PITPs with altered VV-motifs that substitute at least one of the Val residues — typically with at least one bulkier amino acid. While VV-motif polymorphisms do not strongly affect the PtdIns/PtdCho-exchange activities of Sec14 PITPs of virulent fungi, these do confer SMI resistance (21).

Comparison of the SMI-complexed structures reported herein with that of Sfh1 offers a basis for the SMI resistance associated with VV-motif polymorphisms. Sfh1 is a Sec14 paralog that carries the Val Val → Phe Ala polymorphism, does not bind NPPM481, and is resistant to NPPM481 *in vitro* and *in vivo* (20). Our structural studies suggest that the bulky Phe sidechain interferes with NPPM481 and ergoline binding through two mechanisms: (i) partial steric occlusion and (ii) repulsive interactions between the flat face of the aromatic ring (that carries partial negative charge) and the nitro group of NPPM481 and the carbonyl oxygen of the ergoline carboxyester moiety (Fig. 9*B*). Steric incompatibility with SMI binding is also likely in cases such as the *Candida albicans* and *Candida auris* Sec14 PITPs (Val Val → Met Cys and Val Val → Phe Thr polymorphisms, respectively). Thus, rational design strategies aimed at producing pan-fungal Sec14 SMIs could build on a himbacine-fused ring scaffold as a means for circumventing VV-motif polymorphisms. The fact that himbacine adopts a shallow pose in the SMI-binding environment, and does not invade the VV-motif pocket, accounts for why this alkaloid is the only validated SMI to date whose ability to inhibit Sec14 activity is insensitive to VV-motif polymorphisms of virulent fungal Sec14 PITPs.

Future strategies would benefit from improved methods for detecting SMI binding to Sec14. As case in point, our ^{19}F NMR data indicate the close Sec14 paralog Sfh1 and its lipid-activated Sfh1* derivatives fail to detectably bind NPPM481 because of the Val Val → Phe Ala polymorphism, and Sfh1 and Sfh1* are completely resistant to inhibition by NPPM481 *in vitro* and *in vivo* (20, 21). Incorporation of a $Val_{155}Phe$ substitution into the Sec14 context ($Val_{154}Val_{155}$ → Val_{154}-Phe_{155} polymorphism in the VV-motif) is similarly sufficient to endow $Sec14^{V155F}$ with strong resistance to this SMI *in vitro* and *in vivo*. Yet, this $Val_{155}Phe$ substitution reduces apparent NPPM481-binding affinity only ∼12-fold. These data reveal the problematically narrow dynamic range of the *in vivo* and *in vitro* assays currently used to monitor Sec14-SMI interactions. The power of ^{19}F NMR spectroscopy in detecting weak PITP-SMI interactions recommends it as a facile tool for identifying and optimizing lead compounds for the development of next-generation anti-mycotics. This virtue is amply demonstrated by our ability to detect the weak binding interaction between Sec14 and NPPM755—a compound with no detectable inhibitory activity against Sec14 *in vitro* or *in vivo* (20).

Implications for the Sec14 lipid-exchange cycle

Given the significant hydrophobicity of the validated SMIs, the primary mechanism for Sec14 inhibition by SMI involves a 'membrane route' *via* the capture of membrane-embedded SMI. Our data indicate that NPPM481 equilibrates into two pools — a minor aqueous pool and a predominant membrane-incorporated pool (Fig. 9*C*, step 1). The ability of NPPM481 to access the lipid-binding cavity in the absence of membranes suggests that lipid-bound Sec14 exists in equilibrium between closed and open conformers (Fig. 9*C*). Recruitment of Sec14 to membranes can, in principle, occur from either state (Fig. 9*C*, step 2). Release of lipid ligand requires that the membrane-docked Sec14 transition to an open conformer that might be distinct from open conformers that exist in solution. Upon productive membrane binding, the closed Sec14 conformer transitions to the open conformer where bound lipid is released into the bilayer as NPPM481 loads from the membrane into the Sec14 lipid-binding cavity (Fig. 9*C*, step 3). The exchange cycle terminates upon completion of NPPM481 loading and lipid release, transition of Sec14 back to the closed conformer, and disengagement of the PITP from the membrane surface (Fig. 9*C*, step 4). We posit that membranes facilitate formation of the Sec14::NPPM481 complex by increasing the effective SMI concentration *via* efficient solubilization and reduced dimensionality (Fig. 9*C*, step 4).

Regarding the NPPM481 loading reaction, MD experiments project NPPM481 partitions deep into the acyl chain region of the bilayer environment, one characterized by a roughly parallel orientation of the A-ring vector relative to the membrane surface. This configuration suggests that Sec14 must penetrate the acyl chain region of the bilayer to access the SMI. As motion of the amphipathic α10 helix is a major contributor to Sec14 transitions between open and closed conformations, α10 is the most attractive candidate for such deep insertion into the bilayer. This scenario is not consistent with ideas that Sec14 simply captures phospholipid ligands whose headgroups are transiently exposed above the membrane surface. Rather, it supports 'bulldozer' models, such as proposed by Sha *et al.*

(30), that envision Sec14 penetration into the bilayer as a key step in the phospholipid exchange cycle.

Sec14 loading with SMI in membrane-free environments

A surprising result from these studies is the demonstration that aqueous NPPM481 accesses the Sec14 lipid-binding pocket in the absence of membranes. Thus, an alternative pathway for Sec14 inhibition by NPPM481 is *via* invasion of the lipid-binding cavity directly from the aqueous milieu. These data forecast that Sec14 undergoes appreciable conformational dynamics in solution so that the lipid-binding cavity is at least transiently accessible to the SMI in membrane-free contexts (Fig. 9*D*, step 1). Remarkably, this 'solution route' for inhibition results in SMI-mediated displacement of bound PtdCho from its natural binding site and formation of a ternary complex where (i) Sec14 is bound to NPPM481 at its target site and (ii) the displaced PtdCho remains bound in some other configuration in what is likely to be at least a partially open Sec14 conformer (Fig. 9*D*, step 2). The ternary Sec14/NPPM481/PtdCho complex formed in the absence of membranes is particularly intriguing as, upon addition of bicelles, the ternary complex releases the displaced PtdCho into the bilayer and cleanly resolves into an SMI-bound Sec14 product (Fig. 9*D*, step 3).

The ability of the preformed ternary complex to be consumed upon bicelle addition, and resolve into the expected lipid-exchange products, recommends the preformed Sec14::NPPM481::PtdCho complex as a 'productive intermediate' in the exchange cycle. Thus, the structure of this complex is now of interest. In that regard, the open Sec14 conformer bound to NPPM481 exhibits an expansive hydrophobic surface that corresponds to that bound by one of the two β-octylglucopyranoside molecules that infiltrate into the lipid-binding cavity in the original open Sec14 structure ((30); Fig. 9*E*). As this specific β-octylglucopyranoside molecule was successfully used as proxy to identify residues required for PtdIns binding/exchange in the absence of direct structural information (31), and PtdCho and PtdIns assume surprisingly distinct poses in the Sec14 lipid-binding cavity (17), we speculate NPPM481 binding displaces PtdCho into the Sec14 PtdIns-binding site in the ternary complex. We find it an exciting prospect that chemically diverse SMIs might arrest Sec14 at discrete steps of the lipid exchange cycle, thereby facilitating dissection of this unusual mechanism for potentiating PtdIns 4-OH kinase activities and phosphoinositide signaling.

Experimental procedures

Reagents

1-palmitoyl-2-(16-fluoropalmitoyl)-sn-glycero-3-phosphocholine (^{19}F-PtdCho), DMPC, and DHPC were obtained from Avanti Polar Lipids. α,α,α-trifluorotoluene was purchased from Sigma-Aldrich. SMIs were purchased from ChemBridge Chemical Store. The ergoline NGxO4 was kindly provided by Dominic Hoepfner (Novartis), and himbacine was obtained from Santa Cruz Biotechnology, Inc. All SMIs were dissolved in dimethyl sulfoxide (DMSO) to final stock concentrations of 20 to 30 mM and stored in the dark at −20 °C.

Crystallization of Sec14::SMI complexes

Octahistidine-tagged Sec14 (His_8-Sec14) was purified from *Escherichia coli* BL21-CodonPlus (DE3)-RIL cells (Stratagene) as described for Sfh1 (41) with minor modifications. Protein expression was induced with 60 μM IPTG at 16 °C for 20 h. Cells were lysed by glass bead beating in lysis buffer (300 mM NaCl, 25 mM sodium phosphate pH 7.5, and 5 mM β-mercaptoethanol), and the protein was affinity-purified from lysate using Ni-NTA affinity resin (Macherey-Nagel) and elution with imidazole. The His_8-Sec14–enriched fractions were pooled and further resolved into two peaks by size-exclusion chromatography (Superdex 75 16/600 column, GE Healthcare) at a flow rate of 1 ml/min in lysis buffer. Fractions of the slow eluting peak were pooled and concentrated to 5 mg/ml.

All crystallization experiments were conducted at room temperature using a sitting-drop vapor-diffusion method. The drop volumes were 2 μl and consisted of 1 μl Sec14::SMI or Sec14 solution as appropriate and 1 μl of precipitant. Crystals appeared after 2 to 3 days of equilibration. To prepare Sec14::NPPM/NPBB complexes, 5 mg/ml His_8-Sec14 was supplemented with 1 vol% of 20 mM SMI solution in DMSO. The Sec14::NPPM481 and Sec14::NPBB112 crystals were obtained after ∼2 days of equilibration under conditions where the precipitant was comprised of 129.5 mM sodium acetate, 64.8 mM Tris (pH 7.4), 4.6% (w/v) PEG 4000, and 11.9% (v/v) glycerol. The same procedures were applied to crystallize Sec14::NPPM244, except that the glycerol concentration was adjusted to 8.33% (v/v) and pH of the precipitant solution was adjusted to 7.0 with acetic acid.

Crystals of the Sec14::ergoline complex were prepared in two stages. First, apo Sec14 was crystallized by diluting the His_8-Sec14 stock to 2 mg/ml (25 μl of 5 mg/ml His_8-Sec14, 30 μl 5× lysis buffer, and 5 μl lysis buffer). The precipitant composition was 170 mM sodium acetate, 85 mM Tris at pH 6.4, 25% (w/v) PEG 4000, and 11.9% (v/v) glycerol. Second, an ergoline solution containing 0.45 μl precipitant, 0.45 μl 3.33 × lysis buffer, and 0.1 μl ergoline from a 30 mM stock in DMSO was prepared. A 1 μl aliquot of the ergoline solution was directly added to the 2 μl sitting drop containing apo Sec14 crystals in mother liquor followed by an overnight equilibration at room temperature.

To prepare crystals of the Sec14::himbacine complex, a 2 mg/ml His_8-Sec14 solution prepared as described above for the first stage of the Sec14::ergoline crystallization was mixed with 1 vol% of 20 mM himbacine in DMSO. The crystals appeared after a ∼3-days equilibration against precipitant containing 170 mM potassium acetate, 85 mM Tris (pH 7.4, adjusted with acetic acid), 25% (w/v) PEG 4000, and 3.6% (v/v) glycerol.

Structure determination

For data collection, Sec14::NPPM481, Sec14::NPBB112, and Sec14::NPPM244 crystals were transferred to a cryoprotecting

solution (129.5 mM sodium/potassium acetate, 64.8 mM Tris, 10% (w/v) PEG 4000, 20% (v/v) glycerol, pH 7.0) and flash frozen in liquid nitrogen. Sec14::ergoline and Sec14::himbacine crystals were directly flash frozen in liquid nitrogen. Diffraction data were collected at the 10SA (PXII) beamline at the Swiss Light Source (SLS) and indexed, integrated, and scaled using the XDS program package (42). The structures were solved using Molecular Replacement with PHASER (43) using the Sec14::β-octylglucoside structure as search model (PDB entry 1AUA). Subsequent model building was performed in COOT and restrained refinement in PHENIX (44, 45). Ligand restraints were generated with Jligand (46). The quality of the final models was validated with the wwPDB Validation Server (https://validate-rcsb.wwpdb.org/). The coordinates of all structures were deposited in the Protein Data Bank. The accession numbers and statistics are given in Table S1 of the Supporting Information.

Structural analyses and figure preparation were carried out using Visual Molecular Dynamics (VMD) (47), UCSF Chimera (48), CCG Molecular Operating Environment (MOE) (Chem. Comp. Group Inc) (49), and LigPlot$^+$ (50). Chemical structures of SMIs were generated in ChemBioDraw (PerkinElmer).

Computer simulations

NPPM481 parameterization with CHARMM force field

The initial set of CHARMM-compatible force field parameters was obtained with the CGENFF server (51, 52) (Table S2), using the NPPM481 coordinates from the Sec14::NPPM481 crystal structure (PDB entry 7ZGC). Lone particle formalism (53) was used to describe the effect of the Cl 'σ-hole', a small positive charge associated with halogen bonds (54). All internal bond and angle parameters had a low penalty score (<1.5) and were taken as is. Partial charges with penalty scores >2.5 (Fig. S5*A*) and dihedral angles with penalty scores >10 (Fig. S6*A*) were selected for further optimization using the force field Toolkit (ffTK, version 2.1) (55) distributed as the Visual Molecular Dynamics plugin. NPPM481 parameterization followed the standard ffTK workflow and included optimization of geometry, partial charges, and dihedral angles. All quantum mechanical (QM) calculations were conducted using the density functional theory method (56, 57) implemented in Gaussian16 (58). The following levels of theory/basis sets were used for the QM calculations: (i) B3LYP/6-311G++** - initial geometry optimization, (ii) HF/6-31G* - NPPM481–water interaction energies for charge optimization, and (iii) B3LYP/6-311G++** - torsional scan profiles for dihedral angle optimization.

Partial charges were calculated from the NPPM481 water-interaction profiles (Fig. S5, *B* and *C*) and optimized by fitting the molecular mechanics data to the QM-derived dipole moment, water interaction energies, and distances between water and each selected atom (Fig. S5*D*). Good agreement between the molecular mechanics and QM target data is evidenced by low root mean square error values for the water interaction energies and distances (Table S3). Optimization of dihedral angles relied on fitting the potential energy surfaces generated by systematically scanning the dihedral angles and conducting QM calculations of energies for each NPPM481 conformation (Fig. S6, *B*–*E*). For each of the four dihedral angles, quality of fit was evaluated based on the root mean square error values and visual inspection. The optimized partial charges and dihedral angles of NPPM481 are given in Tables S4 and S5.

MD simulations of the Sec14::NPPM481 complex

All atomistic MD simulations were carried out using the Gromacs 2020.4 software package (59) and CHARMM36 all-atom force field (60). The crystal structure of the Sec14::NPPM481 (PDB entry 7ZGC) complex was used as the starting configuration for the MD simulations. The complex was solvated with TIP3P (61) water in a cubic box with an 8 nm edge. 43 Na^+ and 35 Cl^- ions were added to create 100 mM salt concentration and neutralize the charge of the protein complex. After energy minimization, the system was equilibrated for (i) 250 ps under an NVT ensemble at 310.15 K, (ii) 500 ps under an NPT ensemble with protein and ligand restrained, and (iii) 500 ps under an NPT ensemble with protein and ligand unrestrained. Sec14::NPPM481 and solvent (water and ions) were coupled to separate temperature baths at 310.15 K using the V-rescale thermostat with a time constant of 0.1 ps. The pressure was controlled isotropically with the Berendsen barostat algorithm (62) during the NPT equilibration steps and the Parrinello-Rahman barostat algorithm during production runs (63). Long-range electrostatic interactions were treated using the Particle Mesh Ewald method (64) with cubic interpolation and 0.16 nm grid spacing. Molecular bonds were constrained with the LINCS algorithm (65). The short-range neighbor list, van der Waals, and electrostatic cutoffs were all set to 1.2 nm. Periodic boundary conditions were used for all simulations. Randomized starting velocities were assigned from a Maxwell-Boltzmann distribution. Two independent trajectories of 1000 ns were simulated for the Sec14::481 system.

MD simulations of the NPPM481/membrane systems

Four NPPM481-membrane systems were assembled using the CHARMM-GUI membrane builder engine (66). In system 1, NPPM481 was placed 25 Å above the 64 x 64 DMPC bilayer surface. In systems 2-4, 16 NPPM481 molecules were placed at various positions in the 128 × 128 DMPC bilayer:bilayer center (system 2), hydrocarbon region (system 3, 8 molecules per leaflet), and the headgroup region (system 4, 8 molecules per leaflet). All systems were solvated with TIP3P water molecules in rectangular boxes having the dimensions of 6 × 6 × 12 nm (system 1) and 9 × 9 × 12 nm (system 2-4). Eighteen Na^+/Cl^- (system 1) and thirty-nine Na^+/Cl^- ions (system 2-4) were added to create 100 mM salt concentration. Each system was energy-minimized and subjected to the multistage equilibration procedure as prescribed by CHARMM-GUI membrane builder engine. Five hundred ns production runs were executed for each system. Temperature and pressure were controlled using the Nose-Hoover (67, 68) and Parrinello-

Rahman semiisotropic coupling methods, respectively. All other algorithms were as described for the Sec14::NPPM481 simulations.

All MD data were analyzed using the following Gromacs analysis tools: *gmx rmsf* (RMSF analyses); *gmx mindst* (numbers of contacts between two selected atoms/groups), *gmx density* (membrane mass density profiles); *gmx distance* (distances between selected atoms/groups); *gmx gangle* (angles between the NPPM481 A-ring vector and bilayer normal); and *gmx cluster* (cluster analysis). The cluster analysis was conducted using Sec14 residues 13-289, with the cutoff value of 0.2 nm. Contact maps were generated using CONAN software (https://github.com/HITS-MBM/conan) (69).

Preparation of bicelle and protein samples for ^{19}F NMR spectroscopy

All Sec14 NMR experiments were prepared in "NMR buffer 1" at pH 7.2 containing 100 mM NaCl, 25 mM Na_2HP0_4, 0.02% NaN_3, and 8% D_2O. The Sfh1* NMR experiments were prepared in "NMR buffer 2" at pH 7.2 containing 135 mM NaCl, 25 mM Na_2HPO_4, 0.02% NaN_3, and 8% D_2O.

Preparation of bicelles

Isotropically tumbling DMPC/DHPC bicelles (q = 0.5; 36) were prepared as previously described (70). In brief, the appropriate aliquots of DMPC and DHPC solutions in chloroform were dried under vacuum. For ^{19}F-PtdCho–containing bicelles, an aliquot of ^{19}F-PtdCho solution in chloroform was added to create a molar ratio of 1:1067 ^{19}F-PtdCho:(total DMPC + DHPC). The lipid films were resuspended by vortexing in "NMR buffer 1" to create a 1:2 DMPC:DHPC molar ratio and subjected to three freeze-thaw cycles to produce a clear and homogeneous bicelle solution. The stock solution so prepared contained 100 mM DMPC and 200 mM DHPC in case of pure DMPC/DHPC bicelles and 75 μM ^{19}F-PtdCho, 27 mM DMPC, and 53 mM DHPC in case of ^{19}F-PtdCho–containing bicelles. Total lipid concentration was quantified by phosphate assay (71).

Preparation of protein samples

Sec14, its variants Val_{155}Phe and Ser_{173}Cys, and the Glu_{126}Ala variant of Sfh1 (Sfh1*) were expressed in *E. coli* BL21 (DE3) and purified as described in (17, 21) with minor modifications. All protein constructs contained an 8xHistidine tag at the N-terminus. Sec14 and Sfh1 purified from *E. coli* are primarily bound to phosphatidylglycerol (PtdGro) and phosphatidylethanolamine, respectively. After the purification, Sec14::PtdGro and Sfh1::PtdEtn were either exchanged into their corresponding NMR buffers and used as is or, in the case of Sec14 subjected to additional steps, to prepare Sec14::PtdCho, Sec14::^{19}F-PtdCho, and Sec14:NPPM481 complexes.

Preparation of PtdCho-bound Sec14

Purified recombinant Sec14::PtdGro (10 mg) was mixed with sonicated 17 mg POPC in 50 ml of buffer containing 300 mM NaCl, 25 mM Na_2HPO_4 at pH 7.2, and 1 mM NaN_3. The mixture was incubated at 37 °C for 45 min. Sec14::PtdCho was purified on the HisTrap HP column, followed by the gel-filtration chromatography on the HiPrep 16/60 Sephacryl S-100 HR column. The purified Sec14::PtdCho was exchanged into the "NMR buffer 1" for further experiments.

Preparation of ^{19}F-PtdCho–bound Sec14

A 23 μl aliquot of 10 mg/ml ^{19}F-PtdCho was dried under vacuum for 2 h and resuspended in 600 μl of 75 μM Sec14::PtdCho solution in the NMR buffer 1 by gentle vortexing. The resulting mixture was incubated at room temperature overnight. We estimate that 80% of prebound PtdCho was replaced with ^{19}F-PtdCho in Sec14 and will subsequently refer to this preparation as Sec14::^{19}F-PtdCho. The estimate was obtained by comparing the integral ^{19}F NMR peak area of ^{19}F-PtdCho bound to Sec14 with that of the control NMR sample that contained a known amount of ^{19}F-PtdCho in DMPC/DHPC bicelles.

Preparation of NPPM481-bound Sec14

A 100 μl aliquot of 0.5 mM Sec14::PtdGro solution in a buffer containing 300 mM NaCl, 25 mM Na_2HPO_4 at pH 7.2, and 1 mM NaN_3 was mixed with 10 μl of 5 mM NPPM481 solution in DMSO and incubated for 5 min on ice. The mixture was resolved on a Superdex 75 10/300 gel filtration column with Sec14::NPPM481 eluting as a single peak. The peak fractions were pooled, exchanged into the "NMR buffer 1", and concentrated to 45 μM for NMR measurements.

^{19}F NMR experiments

All experiments were conducted on the Avance III Neo NMR instrument (Bruker BioSpin) operating at the ^{1}H Larmor frequency of 600 MHz and equipped with a Prodigy cryoprobe. The temperature was calibrated using methanol-d_4 and set at 25 °C. 1D ^{19}F NMR spectra were collected using the spectral width of 15 ppm and the ^{19}F carrier frequency of either −123.0 or −216.0 ppm. The recycle delay was set to 3 s in all experiments. The number of scans was 2048 and 8192 for the Sec14::PtdCho-NPPM481 spectra of Figure 7, *B* and *C*, respectively, 4096 for the Sec14::PtdCho-NPPM481-bicelle spectra of Figure 5*B*, and 1024 for WT and Sec14 variant spectra of Figure 4, *B*–*D*. All Sfh1* spectra shown in the inset of Figure 4*C* were collected with 128 scans. The spectra of the NPPM755-containing samples (Fig. 4*F*) were acquired with 128 scans for free NPPM755 in solution, 512 scans for NPPM755 in bicelles without Sec14, and 2048 scans for the remaining spectra. To resolve the Sec14-bound resonances of NPPM755 at 1:4 SMI:protein ratio (Fig. 4*F*, inset), a spectrum was collected with 2048 scans, using spectral width of 10 ppm at ^{19}F carrier frequency of -126.8 ppm. All data were zero-filled twice and Fourier-transformed using the 70 Hz Gaussian apodization function, except for the spectra shown in Figure 7, *B* and *C*, where the Gaussian line broadening of 30 and 100 Hz, respectively, were applied. Sfh1* (Fig. 4*C*, inset) and NPPM755 (Fig. 4*F*) data were processed with the Gaussian line broadening of 60 and 20 Hz, respectively.

^{19}F longitudinal relaxation time (T_1) measurements were conducted using 1D inversion-recovery pulse sequence. The experiments were carried out on the Sec14-complexed and DMPC/DHPC bicelle-incorporated ^{19}F-PtdCho, using the recycle delay of 7 s, relaxation delays τ of 0.1, 0.25, 0.5, 1.0, 2.0, and 3.0 s; and 1024 scans per spectrum. The data were zero-filled twice and Fourier-transformed using the 70 Hz Gaussian apodization function. The T_1 values were determined by fitting the data with the following equation:

$$I(\tau) = I_\infty\,(1-2e\,(-\tau/T_1)) \quad (1)$$

where I(τ) is the ^{19}F peak area obtained at the relaxation delay τ and I_∞ is the maximal peak area. The ^{19}F chemical shifts were referenced to the external standard, α,α,α-trifluorotoluene (Sigma-Aldrich) that resonates at −63.72 ppm relative to $CFCl_3$ at 0 ppm. All data processing and analysis was carried out using the MestReNova software package, v.14.2.0.

NMR of binary Sec14::PtdCho-NPPM481 system

The interactions of Sec14-bound PtdCho with NPPM481 were monitored in a series of NMR-detected titration experiments, where increasing amounts of NPPM481 were added from the 7.5 mM stock solution in DMSO-d_6 to the preparation of the Sec14::^{19}F-PtdCho containing 75 μM total protein. The NPPM481 concentrations were 10, 20, 40, 60, 75, and 100 μM. The final sample dilution did not exceed 2%. The data were analyzed using the areas of ^{19}F NMR peaks corresponding to the Sec14-bound ^{19}F-PtdCho (-216.4 ppm); free NPPM481 (-124.5 ppm); and Sec14-bound NPPM481 (-125.9 ppm). At every NPPM481 concentration point, the fraction of Sec14 complexed to PtdCho, $f_{Sec14::PC}$, was calculated from the ratio of the ^{19}F-PtdCho NMR peak areas (PtdCho and NPPM481 are abbreviated to PC and 481 in all equations below):

$$f_{Sec\ 14::PC} = I_{PC} \,/\, I_0 \quad (2)$$

where I_0 and I_{PC} are the areas of the Sec14-bound ^{19}F-PtdCho peak in the absence and presence of NPPM481, respectively. This calculation used the data of Figure 7*B*. The fraction of NPPM481 bound to Sec14, $f_{481,bound}$, was determined using the data of Figure 7*C*:

$$f_{481,bound} = I_{481,bound} \,/\, (I_{481,free} + I_{481,bound}) \quad (3)$$

where $I_{481,free}$ and $I_{481,bound}$ are the areas of the ^{19}F peak corresponding to the free and Sec14-bound NPPM481, respectively. The concentration of Sec14 complexed to NPPM481, [Sec14::481], was calculated as:

$$[Sec\ 14::481] = f_{481,bound} L_0 \quad (4)$$

where $[L]_0$ is the total concentrations of the NPPM481 in the sample. The fraction of Sec14 complexed to 481, $f_{Sec14::481}$, was calculated as the ratio of [Sec14::481] to the total Sec14 concentration.

NMR of ternary Sec14::PtdCho-NPPM481-bicelle system

The protein-NPPM481–binding experiments in the ternary system were conducted in the presence of the DMPC:DHPC bicelles (total lipid 80 mM), using two different types of experiments: (a) titration of Sec14::PtdCho/bicelles with NPPM481 and (b) titration of NPPM481/bicelles with Sec14::PtdGro and its two variants, Ser_{173}Cys and Val_{155}Phe.

In (a), the NPPM481 concentration was 20, 40, 60, 75, 100, and 150 μM. The concentration of the Sec14::481 complex was calculated using the spectra of Figure 5*B* and equations Equations 3 and 4, replacing $I_{481,free}$ with $I_{bic::481}$. The equilibrium constant for the exchange reaction:

$$Sec\ 14::481 + bic \overset{K}{\rightleftarrows} Sec\ 14::PC + bic::481$$

is defined as:

$$K = \frac{[Sec\ 14::PC][bic::481]}{[bic][Sec\ 14::481]} \quad (5)$$

where [bic] and [bic::481] are the concentrations of bicelle lipids and bicelle-bound 481, respectively. Because the total lipid concentration in bicelles, $[bic]_t$ = 80 mM is much larger than the total protein concentration, we can assume that $[bic] \approx [bic]_t$ and redefine the effective equilibrium constant as $K_{eff} = K[bic]_t$. The displacement curve, [Sec14::481] versus L_0, is described by the following equation:

$$[Sec\ 14::481] = 0.5\left[(P_0 + L_0 + K_{eff}) - \sqrt{(P_0 + L_0 + K_{eff})^2 - 4P_0L_0}\right] \quad (6)$$

where P_0 and L_0 are the total concentrations of protein and NPPM481. The P_0 was adjusted to 60 μM to account for active protein in the sample.

In (b), the concentrations of Sec14 variants were 40, 75, 150, and 300 μM, while the concentration of NPPM481 was kept constant at 75 μM. The concentration of Sec14::481 was calculated as:

$$[sec\ 14::481] = f_{481,bound} L_0 = \left[(I_{bic::481,0} - I_{bic::481,p_0}) / I_{bic::481,0}\right] L_0 \quad (7)$$

where L_0 is the total concentration of NPPM481, and $I_{bic::481,0}$ and $I_{bic::481,P0}$ are the ^{19}F-NPPM481 peak areas in the absence and presence of protein, respectively. The binding affinity of NPPM481 to Sec14 variants Ser_{173}Cys and Val_{155}Phe was estimated by fitting the binding curve, [Sec14::481] versus P_0, using Equation 6.

Data availability

The atomic coordinates and structure factors for all Sec14::SMI complexes are deposited in the PDB (https://www.rcsb.org) under the accession codes (SMI) as: 7ZGC (NPPM481), 7ZGD (NPPM244), 7ZGB (NPBB112), 7ZGA (NGxO4), and 7ZG9 (himbacine). Requests for further information should be addressed to the co-corresponding authors.

Supporting information—This article contains supporting information (17, 20, 35).

Acknowledgments—We thank Dominic Hoepfner (Novartis) for providing the NGxO4 used in these studies, Simona Cotesta (Novartis) for providing the Sec14::NGxO4 dock structure, and acknowledge Benjamin Osborn (Biochemistry & Biophysics, Texas A&M University) for his initial involvement in optimizing methods to occupy recombinant Sec14 purified from *E. coli* with PtdCho. We also thank Jae Hyun Cho (Biochemistry & Biophysics, Texas A&M University) for helpful comments and critical reading of the article.

Authors contributions—G. S., F. B., V. A. B., and T. I. I. conceptualization; V. A. B. and T. I. I. writing–original draft; X.-R. C., L. P., Z. H., P. J., S. K., A. T., A. H. N., S. M. G., and D. K. investigation; X.-R. C., L. P., Z. H., S. K., A. T., F. B., V. A. B., and T. I. I. formal analysis; A. H. N. and D. K. validation.

Funding and additional information—This work was supported by grants NIH RO1 GM108998 and NIH R35 GM131804 to T. I. I. and V. A. B., respectively, and award BE-0017 from the Robert A. Welch Foundation to V. A. B. Z. H. and F. B. were supported by the European Research Council under the European Union's Seventh Framework Programme (FP7/2007-2013), ERC grant agreement n° 310957, and the Deutsche Forschungsgemeinschaft (FOR2333). P. J. and G. S. were supported by the Deutsche Forschungsgemeinschaft (DFG, German Research Foundation) under Germany's Excellence Strategy – EXC 2070–390732324 and grant SCHA 1274/4-1 (to G. S.). The content is solely the responsibility of the authors and does not necessarily represent the official views of the National Institutes of Health.

Conflict of interest—The authors declare that they have no conflicts of interest with the contents of this article.

Abbreviations—The abbreviations used are: DHPC, 1,2-dihexanoyl-sn-glycero-3-phosphocholine; DMPC, 1,2-dimyristoyl-sn-glycero-3-phosphocholine; DMSO, dimethyl sulfoxide; MD, molecular dynamics; PITP, phosphatidylinositol transfer protein; PtdCho, phosphatidylcholine; PtdGro, phosphatidylglycerol; PtdIns, phosphatidylinositol; PtdIns-4-P, phosphatidylinositol-4-phosphate; QM, quantum mechanical; SMI, small-molecule inhibitor; TGN, trans-Golgi network.

References

1. Di Paolo, G.,., and De Camilli, P. (2006) Phosphoinositides in cell regulation and membrane dynamics. *Nature* **443**, 651–657
2. Strahl, T., and Thorner, J. (2007) Synthesis and function of membrane phosphoinositides in budding yeast, Saccharomyces cerevisiae. *Biochim. Biophys. Acta* **1771**, 353–404
3. Balla, T. (2013) Phosphoinositides: tiny lipids with giant impact on cell regulation. *Physiol. Rev.* **93**, 1019–1037
4. Dickson, E. J., and Hille, B. (2019) Understanding phosphoinositides: rare, dynamic, and essential membrane phospholipids. *Biochem. J.* **476**, 1–23
5. Bankaitis, V. A., Malehorn, D. E., Emr, S. D., and Greene, R. (1989) The Saccharomyces cerevisiae SEC14 gene encodes a cytosolic factor that is required for transport of secretory proteins from the yeast Golgi complex. *J. Cell Biol.* **108**, 1271–1281
6. Milligan, S. E., Alb, J. G., Jr., Elagina, R., Bankaitis, V. A., and Hyde, D. R. (1997) The phosphatidylinositol transfer protein domain of Drosophila retinal degeneration protein B is required for photoreceptor cell survival and recovery from light stimulation. *J. Cell Biol.* **139**, 351–363
7. Vincent, P., Chua, M., Nogue, F., Fairbrother, A., Mekeel, H., Xu, Y., *et al.* (2005) A Sec14p-nodulin domain phosphatidylinositol transfer protein polarizes membrane growth of Arabidopsis thaliana root hairs. *J. Cell Biol.* **168**, 801–812
8. Giansanti, M. G., Bonaccorsi, S., Kurek, R., Farkas, R. M., Dimitri, P., Fuller, M. T., *et al.* (2006) The class I PITP giotto is required for Drosophila cytokinesis. *Curr. Biol.* **16**, 195–201
9. Ile, K. E., Kassen, S., Cao, C., Vihtehlic, T., Shah, S. D., Huijbregts, R. P. H., *et al.* (2010) The zebrafish class 1 phosphatidylinositol transfer protein family: PITPβ isoforms and double cone cell outer segment integrity in retina. *Traffic* **11**, 1151–1167
10. Huang, J., Ghosh, R., Tripathi, A., Lönnfors, M., Somerharju, P., and Bankaitis, V. A. (2016) Two-ligand priming mechanism for potentiated phosphoinositide synthesis is an evolutionarily conserved feature of Sec14-like phosphatidylinositol and phosphatidylcholine exchange proteins. *Mol. Biol. Cell* **27**, 2317–2330
11. Koe, C. T., Tan, Y. S., Lönnfors, M., Hur, S. K., Low, C. S. L., Zhang, Y., *et al.* (2018) Vibrator and PI4KIIIα govern neuroblast polarity by anchoring non-muscle myosin II. *eLife* **7**, e33555
12. Hamilton, B. A., Smith, D. J., Mueller, K. L., Kerrebrock, A. W., Bronson, R. T., van Berkel, V., *et al.* (1997) The vibrator mutation causes neurodegeneration *via* reduced expression of PITP alpha: positional complementation cloning and extragenic suppression. *Neuron* **18**, 711–722
13. Alb, J. G., Jr., Cortese, J. D., Phillips, S. E., Albin, R. L., Nagy, T. R., Hamilton, B. A., *et al.* (2003) Mice lacking phosphatidylinositol transfer protein-alpha exhibit spinocerebellar degeneration, intestinal and hepatic steatosis, and hypoglycemia. *J. Biol. Chem.* **278**, 33501–33518
14. Xie, Z., Hur, S. K., Zhao, L., Abrams, C. S., and Bankaitis, V. A. (2018) A Golgi lipid signaling pathway controls apical Golgi distribution and cell polarity during neurogenesis. *Dev. Cell* **44**, 725–740
15. Grabon, A., Bankaitis, V. A., and McDermott, M. I. (2019) The interface between phosphatidylinositol transfer protein function and phosphoinositide signaling in higher eukaryotes. *J. Lipid Res.* **60**, 242–268
16. Bankaitis, V. A., Aitken, J. R., Cleves, A. E., and Dowhan, W. (1990) An essential role for a phospholipid transfer protein in yeast Golgi function. *Nature* **347**, 561–562
17. Schaaf, G., Ortlund, E. A., Tyeryar, K. R., Mousley, C. J., Ile, K. E., Garrett, T. A., *et al.* (2008) Functional anatomy of phospholipid binding and regulation of phosphoinositide homeostasis by proteins of the Sec14 superfamily. *Mol. Cell* **29**, 191–206
18. Monteoliva, L., Sanchez, M., Pla, J., Gil, C., and Nombela, C. (1996) Cloning of Candida albicans Sec14 gene homologue coding for a putative essential function. *Yeast* **12**, 1097–1105
19. Chayakulkeeree, M., Johnston, S. A., Oei, J. B., Lev, S., Williamson, P. R., Wilson, C. F., *et al.* (2011) Sec14 is a specific requirement for secretion of phospholipase b1 and pathogenicity of Cryptococcus neoformans. *Mol. Microbiol.* **80**, 1088–1101
20. Nile, A. H., Tripathi, A., Yuan, P., Mousley, C. J., Suresh, S., Wallace, I. M., *et al.* (2014) PITPs as targets for selectively interfering with phosphoinositide signaling in cells. *Nat. Chem. Biol.* **10**, 76–84
21. Khan, D., McGrath, K. R., Dorosheva, O., Bankaitis, V. A., and Tripathi, A. (2016) Structural elements that govern Sec14-like PITP sensitivities to potent small molecule inhibitors. *J. Lipid Res.* **57**, 650–662
22. Pries, V., Nöcker, C., Khan, D., Johnen, P., Hong, Z., Tripathi, A., *et al.* (2018) Target identification and mechanism of action of picolinamide and

benzamide chemotypes with antifungal properties. *Cell Chem. Biol.* **25**, 279–290.e7
23. Hoon, S., Smith, A. M., Wallace, I. M., Suresh, S., Miranda, M., Fung, E., *et al.* (2008) An integrated platform of genomic assays reveals small-molecule bioactivities. *Nat. Chem. Biol.* **4**, 498–506
24. Lee, A. Y., StOnge, R. P., Proctor, M. J., Wallace, I. M., Nile, A. H., Spagnuolo, P. A., *et al.* (2014) Mapping the cellular response to small molecules using chemogenomic fitness signatures. *Science* **344**, 208–211
25. Khan, D., Nile, A. H., Tripathi, A., and Bankaitis, V. A. (2021) Emerging prospects for combating fungal infections by targeting phosphatidylinositol transfer proteins. *Intl J. Mol. Sci.* **22**, 6754
26. Bankaitis, V. A., Tripathi, A., Chen, X.-R., and Igumenova, T. I. (2022) New strategies for combating fungal infections: inhibiting inositol lipid signaling by targeting Sec14 phosphatidylinositol transfer proteins. *Adv. Biol. Reg.* **84**, 100891
27. Bankaitis, V. A., Mousley, C. J., and Schaaf, G. (2010) The Sec14 superfamily and mechanisms for crosstalk between lipid metabolism and lipid signaling. *Trends Biochem. Sci.* **35**, 150–160
28. Smirnova, T., Chadwick, T. G., MacArthur, R., Poluekov, O., Song, L., Ryan, M., *et al.* (2006) The chemistry of phospholipid binding by the Saccharomyces cerevisiae phosphatidylinositol transfer protein Sec14p as determined by electron paramagnetic resonance spectroscopy. *J. Biol. Chem.* **281**, 34897–34908
29. Schaaf, G., Dynowski, M., Mousley, C. J., Shah, S. D., Yuan, P., Winklbauer, E., *et al.* (2011) Resurrection of a functional phosphatidylinositol transfer protein from a pseudo-Sec14 scaffold by directed evolution. *Mol. Biol. Cell* **22**, 892–905
30. Sha, B., Phillips, S. E., Bankaitis, V. A., and Luo, M. (1998) Crystal structure of the Saccharomyces cerevisiae phosphatidylinositol transfer protein. *Nature* **391**, 506–510
31. Phillips, S., Sha, B., Topalof, L., Xie, Z., Alb, J., Clenchin, V., *et al.* (1999) Yeast Sec14p deficient in phosphatidylinositol transfer activity is functional *in vivo*. *Mol. Cell* **4**, 187–197
32. Nile, A. H. (2014) *Chemical Inhibitors of Phosphatidylinositol Transfer Proteins Enable Highly Selective Interference with Specific Pathways of Phosphoinositide Signaling in Cells*, Carolina Digital Repository. University of North Carolina Libraries, Chapel Hill, North Carolina. https://doi.org/10.17615/xdt3-hc64
33. Filipuzzi, I., Cotesta, S., Perruccio, F., Knapp, B., Fu, Y., Studer, C., *et al.* (2016) High-resolution genetics identifies the lipid transfer protein Sec14p as target for antifungal ergolines. *PLoS Genet.* **12**, 1006374
34. Ryan, M. M., Temple, B. R. S., Phillips, S. E., and Bankaitis, V. A. (2007) Conformational dynamics of the major yeast phosphatidylinositol transfer protein Sec14p: insight into the mechanisms of phospholipid exchange and diseases of Secl4p-like protein deficiencies. *Mol. Biol. Cell* **18**, 1928–1942
35. Imai, Y. N., Inoue, Y., Nakanishi, I., and Kitaura, K. (2008) Cl-pi interactions in protein-ligand complexes. *Protein Sci.* **17**, 1129–1137
36. Piai, A., Fu, Q., Dev, J., and Chou, J. J. (2017) Optimal bicelle *q* for solution NMR studies of protein transmembrane partition. *Chemistry* **23**, 1361–1367
37. He, J. J., and Quiocho, F. A. (1991) A nonconservative serine to cysteine mutation in the sulfate-binding protein, a transport receptor. *Science* **251**, 1479–1481
38. Perfect, J. R. (2017) The antifungal pipeline: a reality check. *Nat. Rev. Drug Discov.* **16**, 603–616
39. Fisher, M. C., Hawkins, N. J., Sanglard, D., and Gurr, S. J. (2018) Worldwide emergence of resistance to antifungal drugs challenges human health and food security. *Science* **360**, 739–742
40. Zhang, F., Zhao, M., Braun, D. R., Ericksen, S. S., Piotrowski, J. S., Nelson, J., *et al.* (2020) A marine microbiome antifungal targets urgent-threat drug-resistant fungi. *Science* **370**, 974–978
41. Schaaf, G., Betts, L., Garrett, T. A., Raetz, C. R. H., and Bankaitis, V. A. (2006) Crystallization and preliminary X-ray diffraction analysis of phospholipid-bound Sfh1p: a member of the *Saccharomyces cerevisiae* Sec14p-like phosphatidylinositol transfer protein family. *Acta Crystallogr. F* **62**, 1156–1160
42. Kabsch, W. (2010) Xds. *Acta Crystallogr. Sect. D, Biol. Crystallogr.* **66**, 125–132
43. McCoy, A. J., Grosse-Kunstleve, R. W., Adams, P. D., Winn, M. D., Storoni, L. C., and Read, R. J. (2007) Phaser crystallographic software. *J. Appl. Cryst.* **40**, 658–674
44. Emsley, P., and Cowtan, K. (2004) Coot: model-building tools for molecular graphics. *Acta Crystallogr. Sect. D, Biol. Crystallogr.* **60**, 2126–2132
45. Adams, P. D., Afonine, P. V., Bunko, G., Chen, V. B., Davis, I. W., Echols, N., *et al.* (2010) Phenix: a comprehensive Python-based system for macromolecular structure solution acta crystallographica. *Sect. D, Biol. Crystallogr.* **66**, 213–221
46. Lebedev, A. A.,, Young, P., Isupov, M. N., Moroz, O. V., Vagin, A. A., and Murshudov, G. N. (2012) JLigand: a graphical tool for the CCP4 template-restraint library. *Acta Crystallogr. Sect. D, Biol. Crystallogr.* **68**, 431–440
47. Humphrey, W., Dalke, A., and Schulten, K. (1996) Vmd: visual molecular dynamics. *J. Mol. Graph* **14**, 27–38
48. Pettersen, E. F., Goddard, T. D., Huang, C. C., Couch, G. S., Greenblatt, D. M., Meng, E. C., *et al.* (2004) UCSF Chimera – a visualization system for exploratory research and analysis. *J. Comput. Chem.* **25**, 1605–1612
49. Molecular Operating Environment (MOE) (2018) *2013 08; Chemical Computing Group ULC, 1010*. Sherbooke St West, Suite #910, Montreal, QC, Canada, H3A 2R7
50. Laskowski, R. A., and Swindells, M. B. (2011) LigPlot+: multiple ligand-protein interaction diagrams for drug discovery. *J. Chem. Inf. Model.* **51**, 2778–2786
51. Vanommeslaeghe, K., Hatcher, E., Acharya, C., Kundu, S., Zhong, S., Shim, J., *et al.* (2010) CHARMM general force field: a force field for drug-like molecules compatible with the CHARMM all-atom additive biological force fields. *J. Comput. Chem.* **31**, 671–690
52. Vanommeslaeghe, K., and MacKerell, A. D., Jr. (2012) Automation of the CHARMM general force field (CGenFF) I: bond perception and atom typing. *J. Chem. Inf. Model.* **52**, 3144–3154
53. Pang, Y. T., Pavlova, A., Tajkhorshid, E., and Gumbart, J. C. (2020) Parameterization of a drug molecule with a halogen σ-hole particle using ffTK: implementation, testing, and comparison. *J. Chem. Phys.* **153**, 164104
54. Auffinger, P., Hays, F. A., Westhof, E., and Ho, P. S. (2004) Halogen bonds in biological molecules. *Proc. Natl. Acad. Sci. U. S. A.* **101**, 16789–16794
55. Mayne, C. G., Saam, J., Schulten, K., Tajkhorshid, E., and Gumbart, J. C. (2013) Rapid parameterization of small molecules using the force field toolkit. *J. Comput. Chem.* **34**, 2757–2770
56. Hohenberg, P., and Kohn, W. (1964) Density functional theory (DFT). *Phys. Rev.* **136**, B864
57. Kohn, W., and Sham, L. J. (1965) Self-consistent equations including exchange and correlation effects. *Phys. Rev.* **140**, A1133
58. Frisch, M. J., Trucks, G. W., Schlegel, H. B., Scuseria, G. E., Robb, M. A., Cheeseman, J. R., *et al.* (2016) *Gaussian 16 Rev C 01*, Scientific Research Publishing, Wuhan, China
59. Abraham, M. J., Murtola, T., Schulz, R., Páll, S., Smith, J. C., Hess, B., *et al.* (2015) Gromacs: high performance molecular simulations through multi-level parallelism from laptops to supercomputers. *SoftwareX* **1**, 19–25
60. Huang, J., and MacKerell, A. D., Jr. (2013) CHARMM36 all-atom additive protein force field: validation based on comparison to NMR data. *J. Comput. Chem.* **34**, 2135–2145
61. Jorgensen, W. L., and Jenson, C. (1998) Temperature dependence of TIP3P, SPC, and TIP4P water from NPT Monte Carlo simulations: seeking temperatures of maximum density. *J. Comput. Chem.* **19**, 1179–1186
62. Berendsen, H. J., Postma, J. V., van Gunsteren, W. F., DiNola, A., and Haak, J. R. (1984) Molecular dynamics with coupling to an external bath. *J. Chem. Phys.* **81**, 3684–3690
63. Parrinello, M., and Rahman, A. (1981) Polymorphic transitions in single crystals: a new molecular dynamics method. *J. Appl. Phys.* **52**, 7182–7190

64. Darden, T., York, D., and Pedersen, L. (1993) Particle mesh Ewald: an N·log (N) method for Ewald sums in large systems. *J. Chem. Phys.* **98**, 10089–10092
65. Hess, B., Bekker, H., Berendsen, H. J., and Fraaije, J. G. (1997) Lincs: a linear constraint solver for molecular simulations. *J. Comput. Chem.* **18**, 1463–1472
66. Jo, S., Kim, T., Iyer, V. G., and Im, W. (2008) CHARMM-GUI: a web-based graphical user interface for CHARMM. *J. Comput. Chem.* **29**, 1859–1865
67. Nosé, S. (1984) A molecular dynamics method for simulations in the canonical ensemble. *Mol. Phys.* **52**, 255–268
68. Hoover, W. G. (1985) Canonical dynamics: equilibrium phase-space distributions. *Phys. Rev. A* **31**, 1695
69. Mercadente, D., Gräter, F., and Daday, C. (2018) Conan: a tool to decode dynamical information from molecular interaction maps. *Biophys. J.* **114**, 1267–1273
70. Katti, S., Nyenhuis, S. B., Her, B., Cafiso, D. S., and Igumenova, T. I. (2020) Partial metal ion saturation of C2 domains primes synaptotagmin 1-membrane interactions. *Biophys. J.* **118**, 1409–1423
71. King, E. J. (1932) The colorimetric determination of phosphorus. *Biochem. J.* **26**, 292–297